





## Explaining the origin of the orientation of the front transformation in spin-transition crystals

Nicolas di Scala , Nour El Islam Belmouri , Miguel Angel Paez Espejo, and Kamel Boukheddaden <sup>\*</sup>  
*Université Paris-Saclay, UVSQ, GEMAC, UMR CNRS 8635, 45 Avenue des États Unis, 78035 Versailles, France*

 (Received 27 July 2022; revised 27 September 2022; accepted 4 October 2022; published 25 October 2022)

Preferred orientations of the macroscopic high-spin (HS) low-spin (LS) interfaces appearing in spin transition molecular crystals during their phase transitions are explained through the study of a generalized 3D version of the electroelastic model accounting for an anisotropic change of the lattice parameters,  $a$ ,  $b$ , and  $c$  at the transition. The investigations are performed at 0 K by analyzing the energy landscape of a lattice made of two HS and LS phases, separated by a tilted interface with variable orientation,  $\theta$  as a function of the anisotropy ratio,  $\lambda = \frac{\Delta b}{\Delta a} = \frac{\Delta b}{\Delta c}$ , where  $\Delta x = x_{\text{HS}} - x_{\text{LS}}$  is the lattice misfit along  $x$  ( $= a, b, c$ ) direction between HS and LS states. For large  $\lambda < 0$ , the  $\theta$  dependence of the relaxed total elastic energy depicts a symmetric double-well structure with two stable positions,  $\theta_{\text{min}}$ , and an unstable orientation  $\theta_{\text{max}} = 90^\circ$ . Beyond a critical value,  $\lambda_c^- < 0$ , only one minimum subsists at  $\theta = 90^\circ$ , thus recalling the behavior of an order parameter of a 2nd order phase transition. On increasing  $\lambda$ , this minimum survives until a second threshold value  $\lambda_c^+ > 0$  above which, the elastic energy recovers a double well configuration with two new preferential interface orientations, highlighting the existence of a re-entrant phenomenon. We demonstrate that the behavior of  $\theta_{\text{min}}$  versus  $\lambda$  follows the same universality class as that of a second-order phase transition, for which we calculate the critical exponents  $\beta$  and  $\nu$  through a finite size scaling analysis. Overall, these investigations reveal that in switchable molecular solids with anisotropic unit cell deformation between the LS and HS states, there exists a stress-free interface orientation ensuring their integrity upon a large number of thermal cycles or loads during their practical utilization

DOI: [10.1103/PhysRevB.106.144107](https://doi.org/10.1103/PhysRevB.106.144107)

### I. INTRODUCTION

Spin-crossover materials (SCO) are an interesting class of solids in which molecules exhibit two different spin states: the low-spin (LS) and the high-spin (HS) states [1–3]. SCO solids are transition metals with an electronic configuration ranging between  $3d^4$  and  $3d^7$  (chromium, manganese, iron, and cobalt) which coordinate with (sulphur, oxygen or nitrogen) atoms in octahedral symmetry. In the case of the well-known Fe(II)-based SCO materials with  $3d^6$  configuration, the central transition-metal ion experiences a ligand field energy  $\Delta$  which lifts the degeneracy of the five  $d$  orbitals of Fe(II) and splits them into three weakly bonding and two antibonding orbitals. According to the value of this ligand field and the strength of the interaction between neighboring molecules, a competition rises between two spin states: the diamagnetic low-spin state (LS,  $S = 0$ ) and the paramagnetic high-spin state (HS,  $S = 2$ ). When the value of  $\Delta$  is much stronger (weaker) than the electrons pairing energy, then the central metal ion is in the LS (HS): the transition between the two spin states becomes thermally accessible when  $\Delta \sim k_B T$ , where  $T$  is the temperature. The volume of the molecules changes between these two spin states, becoming larger in the HS state, and is accompanied by a collective transition in the solid state. While the LS state is energetically privileged at low temperature, the HS state is favoured at high temperatures due to entropy effect. The spin transition can be induced by several

external parameters such as changes in temperature [2,4,5], external pressure [6–8], magnetic field [9,10], or light irradiation (via LIESST effect, standing for light induced excited spin state trapping; which is trapping at low temperature of HS metastable state by light) [11–14]. The HS-LS transition produces various changes in properties including structural, magnetic, vibrational and optical changes at the transition. This peculiar bistability is an essential feature for applications of these switchable molecular solids such as molecular switches, data storage or display devices [15–17]. Depending of the intensity of the elastic interactions between molecules, various thermally induced spin transitions can emerge, going from continuous gradual transitions [18] to first-order hysteretic ones [19]. To gather information about cooperativity of the system, the evolution of the HS fraction  $n_{\text{HS}}$  relative to some interesting parameters is used to describe the spin state of the system. Several theoretical models have been developed to explain cooperativity and to make links with the transition [20–23]. One of the various fruitful models, considering the lattice volume change at the transition, is the electroelastic models class [24,25], which have been proven useful to clarify experimental spatiotemporal behaviours of the transition observed by optical microscopy in spin transition materials [26–28]. In these models, SCO molecules are modeled by fictitious spin states  $S_i$  having two values, +1 (for HS) and –1 (for LS), occupying the lattice nodes at position coordinates  $(x, y, z)$  and interacting with their neighbors through springs, whose elastic constants depend on the spin states of the connected spins. Numerical simulations have been performed mainly on two-dimensional (2D) systems [24,29–33],

<sup>\*</sup>kamel.boukheddaden@uvsq.fr

however, three-dimensional (3D) models appear progressively [34–36].

In a previous 3D study [37], we showed that for thermally induced transition, as well as at low temperature isothermal relaxation, the HS-LS interface is perpendicular to its propagation axis in a rectangular crystal with the orientation angle of the HS-LS interface  $\theta = 90^\circ$ . On the other hand, since ten years, the development of observation techniques, particularly through optical microscopy (OM) method allowed evidencing the presence of macroscopic spin domains with HS and LS interfaces with various shapes and kinetics changing from one single crystal to another, and very sensitive to the structural quality of the observed crystal. In most of the crystals, the first switching of the material creates irreversible defects ending the experience. The strains at work in the material are clearly identified as due to the volume change (some percent) inherent to the spin transition. Among the rare exceptions to this disappointing behavior, the compound  $[\{\text{Fe}(\text{NCSe})(\text{py})_2\}_2(m\text{-bpyz})]$  [14,27,38–43], where  $\text{py} = \text{pyridine}$  and  $\text{bpyz} = 3,5\text{-bis}(2\text{-pyridyl})\text{pyrazolate}$ , provided robust single crystals able to undergo til 100 thermal cycles without any noticeable structural fatigue. In this crystal, the straight HS/LS interface observed in fine and thin crystals of high quality, showed two privileged orientations, obviously related to the structural changes involved along the spin transition. In all the large number of studied crystals of this material, the angles of the interface orientations relative to the propagation axis, have been evaluated to  $\theta = 60^\circ$  and  $120^\circ$ . These values are very stable and changes by only some degrees from one single crystal to another, indicating the existence of a common character to all crystals belonging to this material, whatever their sizes and shapes. In a more recent work [38], however, it was demonstrated that the macroscopic crystal bending may affects the stable interface orientation, which confirms that the emergence of these two stable orientations has a structural origin. A 2D anisotropic electroelastic model has thus been developed in Refs. [38,39], associating the existence of these two symmetric interface orientations with the anisotropy of deformation of the unit cell along the thermal spin transition.

Our previous 3D study [37] predicting an interface angle  $\theta = 90^\circ$  was based on an isotropic description of the 3D electroelastic model, where the lattice changes along the spin transition are so that,  $\Delta a = \Delta b = \Delta c$ , where  $a$ ,  $b$ , and  $c$  are the three crystalline directions. Here, we carry out numerical simulations on an anisotropic electroelastic model for 3D lattice, with,  $\Delta a \neq \Delta b \neq \Delta c$ . The considered anisotropy is generated on the elementary cell by modifying the equilibrium distances between first neighbors ( $1n$ ) of the connected spins, relative to the three  $a$ ,  $b$  and  $c$  directions. In this work, we explore the energetic stability of the orientation  $\theta$  of the HS-LS interface as a function of the anisotropy ratio  $\lambda$ , which also measures the elastic frustration rate between the three directions of the elemental cell.

Numerically, we freeze the electronic degrees of freedom of the lattice, and we use molecular dynamics algorithm to let the structural degrees of freedom evolve: thus, the system can only be mechanically relaxed, in order to reach equilibrium such as in [44]. We implement this process thanks to the Compute Unified Device Architecture (CUDA Nvidia) [45]

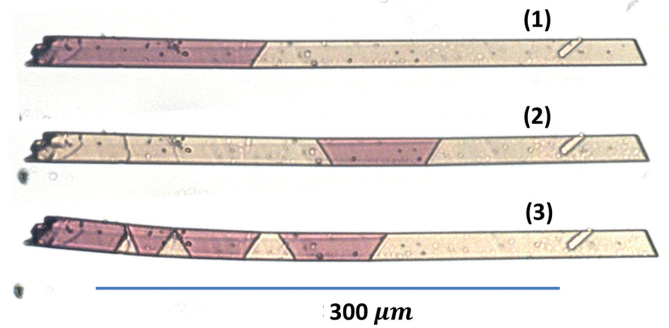


FIG. 1. Top view of a thin crystal of the compound  $[\{\text{Fe}(\text{NCSe})(\text{py})_2\}_2(m\text{-bpyz})]$ , along the thermal spin transition from the HS spin (light region) to the low-spin (dark region) at 105 K (1) and in several conditions of photothermal conditions (in vacuum, intensely illuminated) for a bath temperature  $\sim 75$  K (2, 3). In all snapshots, we see the appearance on thin and tilted HS-LS interface with two preferred orientations at  $60^\circ$  and  $120^\circ$  with respect to the propagation direction. In (3), the crystal bending causes the appearance and the coexistence of multiple HS-LS domains.

allowing us to improve computation time of our simulations and to reach larger lattice's size.

This manuscript is structured as follows: in Sec. II, we present the experimental interface and the 3D electroelastic model with the numerical ingredients; Sec. III display the results obtained from these simulations, in Sec. IV, we conclude.

## II. EXPERIMENTAL INTERFACE AND 3D ANISOTROPIC ELECTROELASTIC MODEL

### A. The experimental interface

An example of a snapshot of a thin single crystal of compound  $[\{\text{Fe}(\text{NCSe})(\text{py})_2\}_2(m\text{-bpyz})]$  obtained by optical microscopy measurements along the thermal spin transition [39] is depicted in Fig. 1. Three snapshots, labeled (1)–(3), are presented. Snapshot (1), taken in the course of the phase transition, shows the formation of the LS phase (dark area) along the cooling process from the HS phase (light area), where the corresponding switching temperature is 105 K. The LS phase starts from the left tip of the crystal and propagates towards the right corner in the form of a single domain. Once the LS state nucleates from one corner of the crystal, it prevents other nucleation from the other corner. In addition, in all OM experiments, the nucleation never starts from the center of the lattice, which reveals that the spin transition is stress-driven mechanism. Snapshot (1) also indicates that the front interface is made of a thin line, tilted with an angle of  $60^\circ$  with respect to the crystal length. Snapshot (2) is obtained from (1) by increasing the light intensity of the microscope lamp, which causes the photoheating of the crystal. Thus the crystal temperature in (2) is much higher than that of the thermal bath (or cold finger of the cryostat). As a result, the already transformed LS phase in the left region of snapshot (1) transforms into a HS phase, starting from the left tip of the crystal. A LS domain with symmetric interfaces orientations ( $120^\circ$  and  $60^\circ$ ) becomes trapped between two big HS domains, which indicates that the HS-LS interface has two possible

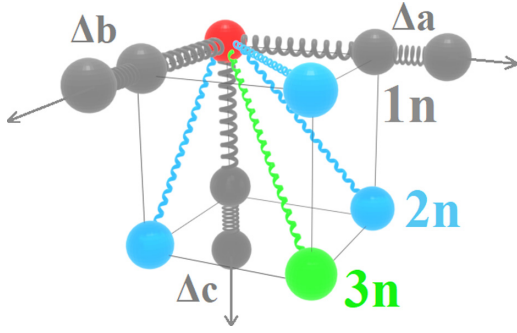


FIG. 2. 3D elastic network scheme in a unit cell simulation. A test site is represented in red, while its neighbors are represented in grey for the nearest neighbors ( $1n$ ), in blue for the next-nearest neighbors ( $2n$ ) and in green for the next-next-nearest neighbors ( $3n$ ). Springs of the same color are visible to illustrate the connections between spins. Representation of the anisotropic unit cell's change is shown through the lattice constant misfit  $\Delta a$ ,  $\Delta b$ , and  $\Delta c$  between the HS and LS lattices along respectively  $a$ ,  $b$ , and  $c$  directions.

and symmetric orientations. Finally, the third snapshot (3) shows an interesting situation demonstrating that the crystal bending, which happened here spontaneously, after several illuminations, causes the appearance of multiple coexisting HS-LS domains separated by interfaces which always have the two previously presented preferential orientations. These behaviors denote that these orientations have a microscopic origin, and are directly related to the unit cell change between the LS and the HS states. Indeed, x-ray diffraction investigations, provided in Ref. [39], showed that during the spin transition from LS to HS, for which the total volume increases, the unit cell parameters exhibit anisotropic deformations, with an expansion along  $a$  and  $c$  directions and a contraction along  $b$  direction. This behavior is identified as the key parameter of the existence of two stable interface orientations, minimizing the lattice strain in the material. The objective of the present model is to demonstrate that this conjecture is correct.

### B. Anisotropic model

We consider a 3D anisotropic version of the electroelastic model: the HS and LS states are described by a two-states fictitious spin  $S_i$ . The eigenvalues  $S_i = +1$  and  $S_i = -1$  are associated with the HS and LS states, respectively, for the  $i$ th molecule of the lattice. We bind each molecule to its neighbors via an elastic spring. The anisotropy is introduced through the equilibrium distances of the nearest neighbors ( $1n$ ) which depend on the direction of space, while for the next-nearest neighbors ( $2n$ ) and next-next-nearest neighbors ( $3n$ ) equilibrium distance depends only on the connected spin states and change in the isotropic way. As illustrated in Fig. 2, the  $1n$  neighbors are located along the edges of the cube, while the  $2n$  are along the diagonals of the faces and the  $3n$  along the long diagonals of the elementary cell. Equilibrium distance between two neighboring HS sites is naturally brought greater than that between two LS sites.

The total ‘‘Hamiltonian’’ of the system is defined by

$$H = \sum_i (\Delta - k_B T \ln g) S_i + H_{\text{elast}}, \quad (1)$$

TABLE I. Values of the nearest-neighbor ( $1n$ ) equilibrium lattice parameters used for the anisotropic unit cell's change. Only  $b_{HH}$  is variable while the others lattice constants are kept invariant.

$1n$ distances ( $nm$ )		
along $x$ direction	$a_{HH} = 1.20$	$a_{LL} = 1.00$
along $y$ direction	$b_{HH}$	$b_{LL} = 1.00$
along $z$ direction	$c_{HH} = 1.20$	$c_{LL} = 1.00$

where the temperature-dependent ( $\Delta - k_B T \ln g$ ) term of Eq. (1) represents the effective ‘‘ligand field’’ electronic contribution, accounting for the ligand field energy gap  $\Delta$  and the degeneracy ratio  $g = g_{\text{HS}}/g_{\text{LS}}$  between HS and LS states, which plays the role of an entropic term.  $T$  is the temperature and  $k_B$  is the Boltzmann constant. The  $H_{\text{elast}}$  term represents the elastic energy of the lattice defined by

$$\begin{aligned} H_{\text{elast}} &= V_{1n}(|\vec{r}|) + V_{2n}(|\vec{r}|) + V_{3n}(|\vec{r}|) \\ &= A_{1n} \underbrace{\sum_{(i,j)} (r_{ij} - d_{1n}(S_i, S_j))^2}_{1n \text{ neighbors}} \\ &\quad + B_{2n} \underbrace{\sum_{(i,k)} (r_{ik} - d_{2n}(S_i, S_k))^2}_{2n \text{ neighbors}} \\ &\quad + C_{3n} \underbrace{\sum_{(i,p)} (r_{ip} - d_{3n}(S_i, S_p))^2}_{3n \text{ neighbors}}. \end{aligned} \quad (2)$$

The elastic constants connecting a site to its neighbors are defined by  $A_{1n}$  for  $1n$  neighbors,  $B_{2n}$  for  $2n$  neighbors, and  $C_{3n}$  for  $3n$  neighbors. Euclidean distances are given by  $r_{ij}$  (respectively  $r_{ik}$  and  $r_{ip}$ ) between the  $1n$  sites  $i$  and  $j$  (respectively between  $2n$  sites  $i$  and  $k$ , and  $3n$  sites  $i$  and  $p$ ). Equilibrium bond lengths between two  $1n$  sites is  $d_{1n}(S_i, S_j)$ ,  $d_{2n}(S_i, S_k)$  between two  $2n$  sites and  $d_{3n}(S_i, S_p)$  between two  $3n$  sites. We indicate by  $a_{HL}$  (respectively  $b_{HL}$ ,  $c_{HL}$ ),  $a_{LL}$  (respectively  $b_{LL}$ ,  $c_{LL}$ ),  $a_{HH}$  (respectively  $b_{HH}$ ,  $c_{HH}$ ), equilibrium distances between  $1n$  HS-HS, LS-LS, and HS-LS configurations along the  $x$  direction (respectively  $y$  and  $z$  directions): we have  $a(+1, +1) = a_{HH}$ ,  $a(-1, -1) = a_{LL}$ ,  $a(+1, -1) = a(-1, +1) = a_{HL}$  and similarly for  $b$  and  $c$  parameters. We summarize in Table I the values of the equilibrium lattice parameters used for the anisotropic unit cell's change. The equilibrium distances between  $2n$  and  $3n$  depend on the state of the linked spins by the formula

$$\begin{aligned} d_{1n}(S_i, S_j) &= R(S_i, S_j), \\ d_{2n}(S_i, S_k) &= \sqrt{\phi^2(S_i, S_k) + \psi^2(S_i, S_k)}, \end{aligned} \quad (3)$$

$$d_{3n}(S_i, S_p) = \sqrt{a^2(S_i, S_k) + b^2(S_i, S_k) + c^2(S_i, S_p)}, \quad (4)$$

where  $R(S_i, S_j) = \{a(S_i, S_j), b(S_i, S_j), c(S_i, S_j)\}$  is the equilibrium nn distance along the three directions,  $a$ ,  $b$ , are  $c$ , while  $\phi$  or  $\psi$  are the pair distances along the diagonals of the faces between  $1n$  and  $2n$  ( $\{\phi, \psi\} = \{a, b, c\}$ ), and the general formula is given by  $\phi(S_i, S_j) = \phi_{HL} + \frac{\Delta\phi}{4}(S_i + S_j)$ ,

$\forall(i, j)$ . Simulations performed in this paper have been done with the parameter values:  $\Delta = 450$  K and  $g = 150$  leading to the equilibrium transition temperature of the Ising-like model  $T_{eq} = \frac{\Delta}{k_B \ln g} \approx 90$  K and entropy change  $\Delta S = R \ln(g) \approx 42 \text{ J K}^{-1} \text{ mol}^{-1}$ , where  $R$  is the perfect gas constant. The isotropic elastic constants used is  $A_{1n} = 3000 \text{ K nm}^{-2}$ , leading to a bulk modulus  $E \approx \frac{A_{1n}}{R_0} \approx 5$  GPa, which is in quite good agreement with those reported in literature [46]. For simplicity, we arbitrary choose  $B_{2n} = C_{3n} = 0.3 A_{1n}$  for second and third neighbors, whose essential role here is to maintain the stability of the lattice, and we assume that  $a_{HL} = \frac{(a_{HH} + a_{LL})}{2}$  and similarly for  $b$  and  $c$ , so that comparisons can be done with previous study at 3D [37].

The anisotropic unit cell's change is revealed through the lattice constant misfit  $\Delta a = a_{HH} - a_{LL}$ ,  $\Delta b = b_{HH} - b_{LL}$ , and  $\Delta c = c_{HH} - c_{LL}$  between the HS and LS lattices along respectively  $a$ ,  $b$  and  $c$  directions. We define the anisotropy ratio parameter  $\lambda = \frac{\Delta b}{\Delta a} = \frac{\Delta b}{\Delta c}$ , which will be a tunable parameter in our simulations allowing to modify the rate of the anisotropy introduced in the lattice. We have chosen to monitor only the lattice parameter  $b_{HH}$ , allowing only  $\Delta b$  to change, and we opt for the same equilibrium lattice parameter along the  $a$  and  $c$  direction. Therefore anisotropy can occur in the  $b$  direction:  $\frac{\Delta a}{\Delta c} = 1$ . This choice has been done to approach what has been observed experimentally in  $[\{\text{Fe}(\text{NCSe})(\text{py})_2\}_2(m\text{-bpy}p\text{z})]$ , as previously discussed, where during LS-HS transition a contraction along one direction and an expansion along another direction can be achieved. Because of this choice, there will be three different situations for the anisotropic unit cell's change: for  $\lambda < 0$ , the unit cell contracts along the  $b$  direction, when the crystal converts from LS to HS, while along the  $a$  and  $c$  directions it stretches. For  $\lambda > 0$ , the unit cell stretches along the three directions, but in anisotropic way: smaller expansion along the  $b$  direction relative to the  $a$  and  $c$  directions for  $0 < \lambda < 1$ , and bigger expansion along the  $b$  direction relative to the two others directions for  $\lambda > 1$ . The isotropic expansion (contraction) case is indeed obtained for  $\lambda = 1$ .

### C. Numerical ingredients

We have implemented a CUDA code (Compute Unified Device Architecture - Nvidia), letting us to do massive parallel simulations, and improving the size of our simulation cells, with a reasonable computational time. The graphic card used is a Nvidia RTX A5000 based on the Ampere architecture with 8192 cores, 24 GB GDDR6 memory available, a single precision performance up to 27.8 TFLOPS, and the CUDA driver version installed is 11.4.

We compute 3D parallelepipedic lattices of size  $(N_x \times N_y \times N_z)$  with free boundary conditions allowing the lattice to expand/contract and to distort. We choose reasonable sizes in the three directions of space, to keep acceptable computational time without effect on physical quantities, with  $N_x \in [16, 192]$ ,  $N_y \in [16, 72]$ , and  $N_z \in [16, 72]$ . We will show in a further paragraph the influence of the lattice size on the results, and we will confirm then the legitimate choice of sizes.

When the code is executed, CUDA generates a grid of threads that are organized in a three-dimensional hierarchy.

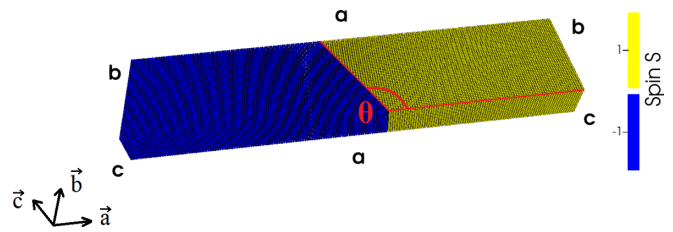


FIG. 3. Example of spatial configuration of the fixed HS-LS phases for a lattice of size  $(192 \times 48 \times 16)$  with an orientation of the interface  $\theta = 120^\circ$  with respect to the  $a$  direction. Yellow (blue) spheres represent HS (LS) sites.

Each grid is organized into an array of thread blocks, where each one can contain up to 1024 threads and thread block size should be a multiple of 32 due to the multiprocessor of the cards which can create, manage, schedule, and execute threads in groups of 32 parallel threads called warps. For each chosen simulation size of the system, the thread block size has to be well defined for a better efficiency. Thus very small block sizes, e.g., 32 threads per block, may limit performance due to occupancy, whereas very large block sizes, for example, 1024 threads per block, may also limit performance. Each site of the lattice represents a spin-crossover molecule whose degrees of freedom are defined by its spin value  $\pm 1$  and its coordinates  $(x, y, z)$  in the lattice. The entire lattice is divided into sublattices which are then mapped onto thread blocks, where each of the sublattice/block contains  $(16 \times 4 \times 4) = 265$  threads, representing 256 molecules, that are also called sites through the paper. Overall, this forms a three-dimensional grid of  $(6 \times 8 \times 8) = 384$  thread blocks. These blocks are contiguous, as the sites inside each block: we subdivide the lattice into multiple blocks in order to improve the computational time. Our GPU can perform operations on up to 8192 threads simultaneously. Indeed, the GPU is built on an array of Streaming Multiprocessors (64 in our case), where each Streaming Multiprocessors has a total of 128 cores and performs operations on only one thread block at a time. Also the order in which thread blocks are scheduled on the Streaming Multiprocessors is decided by the hardware at runtime. Indeed, in CUDA each block of threads is scheduled (independently from the others) on any of the available multiprocessors within the GPU, in any order, concurrently or sequentially, so that the program can be executed on the maximum number of multiprocessors.

As depicted in Fig. 3, we define two fixed spin states phases in the lattice with a tilted HS-LS interface separating these two phases. The orientation  $\theta$  of the interface is measured between the  $a$  direction and the interface. Furthermore, the interface is kept always perpendicular to the plane  $(a, b)$ . It would be interesting to study the impact of the angular orientation of the interface with respect to the plane  $(a, b)$ , we let this for a later study.

As discussed formerly, the present study is done to reproduce the experimental results of optical microscopy of  $[\{\text{Fe}(\text{NCSe})(\text{py})_2\}_2(m\text{-bpy}p\text{z})]$  displaying tilted HS/LS interfaces with two symmetric angles with respect to the crystal length. The interface crosses the center of the 3D simulation cell, giving thus a value of  $n_{HS} = 0.5$  (as many HS as LS sites).

### 1. Initial electronic and structural states and lattice relaxation procedure

The lattice is initially set with all of the  $1n$ ,  $2n$ , and  $3n$  equilibrium distances equal to those of the HS state. This means that from the structural point of view, the lattice is set in the HS phase:  $r_{ij}^x = a_{HH}$ ,  $r_{ij}^y = b_{HH}$ ,  $r_{ij}^z = c_{HH}$ , where  $r_{ij}^x$  (respectively  $r_{ij}^y$ ,  $r_{ij}^z$ ) is the instantaneous distance along the  $x$  (respectively  $y$  and  $z$ ) direction. On the other hand, the half left (respectively right) part of the lattice represented in blue (respectively yellow) is set with a spin value  $S = -1$  (respectively  $S = +1$ ) corresponding to the LS (respectively HS) electronic state. Thus, initially, the lattice experiences a high elastic strain in the left part, in which antagonist electronic and structural configurations are imposed initially, while in the right part, the system is in the HS state from both electronic and structural point of view. Consequently, it is expected in the course of the simulations that the LS part reacts first in an explosive way so as to minimize the initial injected strain. To solve the Hamiltonian of Eq. (2), since the spins are not allowed to change their value, only the structural degrees of freedom (lattice positions) are allowed to evolve via a molecular dynamics (MD) algorithm where the elastic relaxation is made by classical mechanics by solving Newton's equations at 0 K while imposing a strong viscosity to avoid oscillations. Instead of using a numerical parameter for the damping factor, we impose  $V_i = 0$  for the speed of all sites after each step of simulation. More precisely at each time step, the gradient of potential energy of each site is calculated in order to evaluate the force vector  $\vec{F}_i = -\vec{\nabla}H_i$  acting on every particle. The obtained forces are then renormalized by dividing by the highest one (denoted  $F_{\max}$ )  $\vec{f}_i = \vec{F}_i/F_{\max}$ , which are then multiplied by  $\delta t$  to calculate the velocities  $\vec{V}_i = \vec{f}_i \times \delta t$ , which are in turn used to determine the new positions of all particles  $\vec{r}_i = \vec{V}_i \times \delta t + \vec{r}_0 = \vec{f}_i \times \delta t^2 + \vec{r}_0$ , where  $\delta t^2 = 0.001$ . This procedure is repeated until getting to the equilibrium state, which can be controlled with the time dependence of the total elastic energy of the system which reaches a minimum averaged value or a zero total force acting on each site.

## III. RESULTS

### A. Anisotropy ratio $\lambda < 0$

Hereafter, we will focus primarily our attention on the peculiar case of anisotropy  $\lambda < 0$  where the unit cell contracts along the  $b$  direction and stretches along the  $a$  and  $c$  directions along the LS to HS transition. This choice is made to get closer to experimental reality, like it has been observed in  $[\{\text{Fe}(\text{NCSe})(\text{py})_2\}_2(m\text{-bpypz})]$ , where the anisotropic deformation of the SCO unit cell exhibited  $\lambda < 0$ .

#### 1. Energy angular dependency

For each anisotropy ratio value  $\lambda$ , we select several  $\theta$  values in the interval  $\theta \in [20^\circ, 160^\circ]$ , then for each one, we let the lattice relax mechanically to reach asymptotically the stable mechanical state. The value of the total elastic energy  $\langle E \rangle$  of the system is measured after relaxation, and we reiterate the relaxation for a new different fixed  $\theta$  value, looking for the energetically preferential orientation of the HS-LS

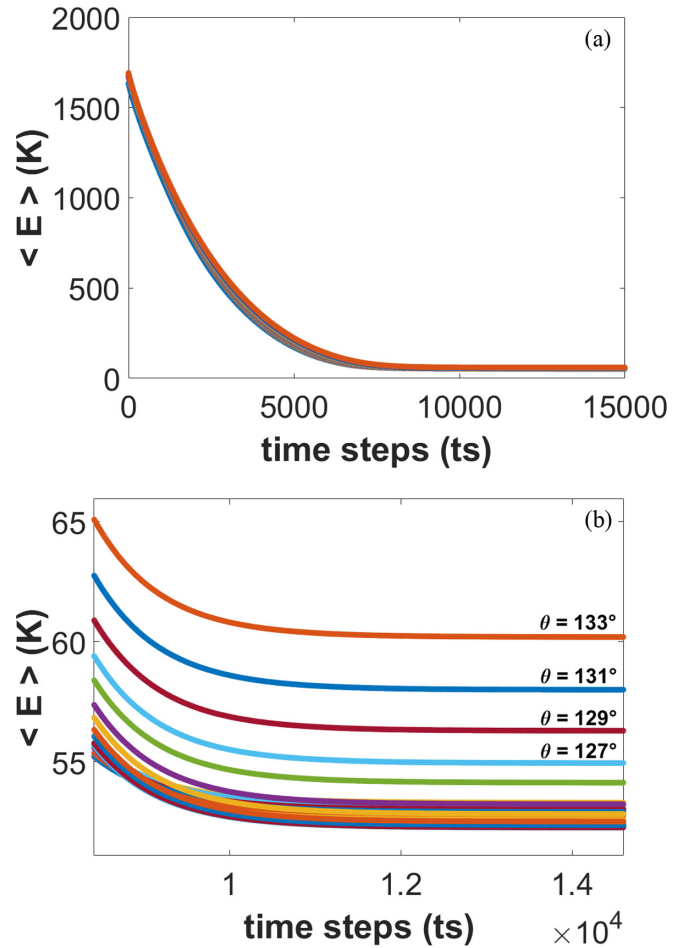


FIG. 4. Time evolution (in time steps units (ts)) of the total elastic energy  $\langle E \rangle$  (K) of the system for the case of  $(48 \times 48 \times 48)$  and  $\lambda = -0.5$ . Each colored plot correspond to a fixed  $\theta$  value between  $20^\circ$  and  $160^\circ$ . Remark that the minimal averaged value is non zero, because of the HS-LS interface. The lattice relaxation deforms the lattice but does not modify the interface orientation. (a) Overview of the time evolution of  $\langle E \rangle$ ; (b) zoom on the time evolution of  $\langle E \rangle$  around the stationary states where the top curve corresponds to  $133^\circ$  and the bottom one to  $113^\circ$  with an angle step  $\Delta\theta = 2^\circ$  separating two curves from top to down.

interface. Figure 4 displays typical results obtained for the time evolution of  $\langle E \rangle$ , here for the case of  $(48 \times 48 \times 48)$  and  $\lambda = -0.5$ . In Fig. 4(a), we present an overview of  $\langle E \rangle$  reaching a minimal averaged value, and in Fig. 4(b), a zoom on the asymptotical reaching of the latter. We observe that higher curves in energy on the graphic correspond to edge values of the orientation  $\theta$  of the interface (around  $20^\circ$  and  $160^\circ$ ). Furthermore, we notice that curves are symmetrically distributed in energy around the value  $\theta = 90^\circ$ , which is the interface orientation perpendicular to  $a$  direction: curves at  $90^\circ \pm |\theta - 90^\circ|$  are overlaid on each other. We can mention that the minimal averaged value  $\langle E \rangle$  is non zero, because of the HS-LS interface storing elastic energy, and involving a residual strain inside the lattice, as explained previously [37].

Because of the symmetrical distribution in energy around  $\theta = 90^\circ$ , we draw the energetic landscape  $\langle E \rangle$  relative to  $\theta$  for each studied anisotropy ratio value  $\lambda$ , as illustrated in Fig. 5

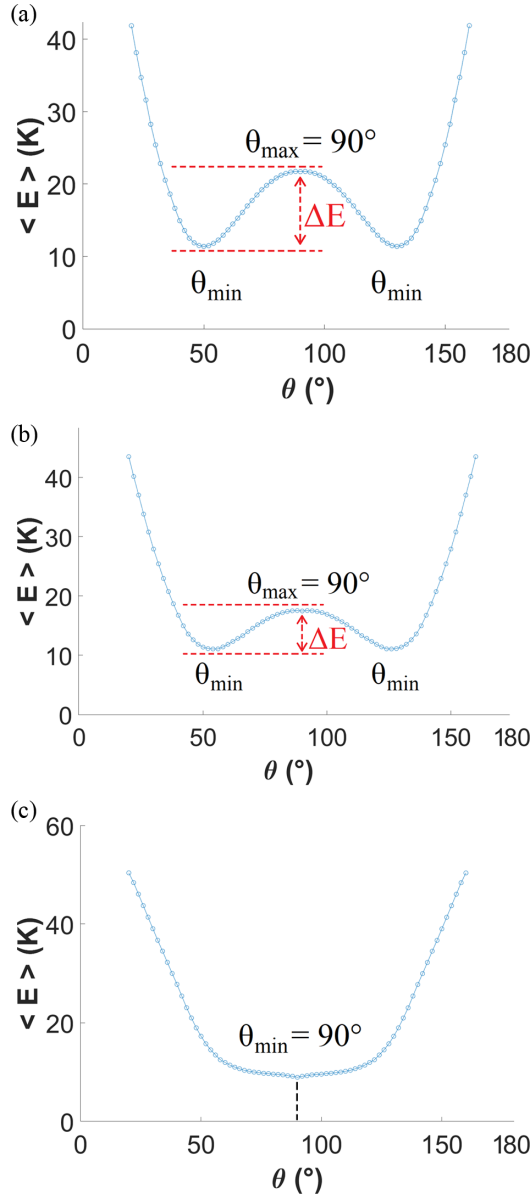


FIG. 5. Energetic landscape  $\langle E \rangle$  (K) relative to  $\theta$  (degrees) for different anisotropy ratio values  $\lambda$  for the case of  $(96 \times 96 \times 16)$ . In red is represented the height of the energy barrier  $\Delta E$  (K) between peak values  $\theta_{\max}$  and  $\theta_{\min}$  for different  $\lambda$  values. (a)  $\lambda = -0.6$ , (b)  $-0.5$ , and (c)  $-0.1$ .

for the typical case  $(96 \times 96 \times 16)$  which is representative of what we obtain for all of our simulation sizes. We note that this energy landscape has a double well structure for large negative  $\lambda$  [Figs. 5(a) and 5(b)], where the two minima  $\theta_{\min}$  (isoenergetic) correspond to stable positions of the interface, while the  $\theta_{\max} = 90^\circ$  maximum corresponds to an unstable position. However, beyond a critical value of the anisotropy ratio the situation is transformed and only one minimum survives  $\theta_{\min} = 90^\circ$  [Fig. 5(c)].

## 2. Relaxed spatiotemporal configurations and local pressure field

We display in Fig. 6 the spatial configurations of the lattice and the corresponding distribution of the local pressure

field, for the initial configuration ( $t = 0$ ) and the relaxed one ( $t = 34\,650$  ts), for the simulation size  $(96 \times 96 \times 16)$  and  $\lambda = -0.6$  at  $\theta_{\max} = 90^\circ$  in Fig. 6(a) and at  $\theta_{\min} = 130^\circ$  in Fig. 6(b). The local pressure,  $P_i$  at site  $i$ , is calculated by the following expression:

$$P_i = -A_{1n} \sum_j (r_{ij} - d_{1n}(S_i, S_j)) - B_{2n} \sum_k (r_{ik} - d_{2n}(S_i, S_k)) - C_{3n} \sum_p (r_{ip} - d_{3n}(S_i, S_p)). \quad (5)$$

This physical quantity is interesting because the local pressure may be positive or negative according to the stress applied on the site: a compressive strain is equivalent to a positive pressure exerted on the site, while a tensile strain results in a negative pressure.

We observe from the two relaxed spatial configurations of Fig. 6 that the sublattice of the LS state phase stretches along the  $b$  direction and contracts along the  $a$  and  $c$  directions, which is coherent since the whole lattice was initially set with all of the  $1n$  equilibrium distances equal to those of the HS state, imposing the sublattice of the LS state phase to reach its equilibrium position during the relaxation process. Because  $\Delta a > 0$  and  $\Delta c > 0$ , then  $\lambda < 0$  imply  $\Delta b < 0$  meaning that  $b_{HH} < b_{LL}$ , it corresponds to a stretching along the  $b$  direction in the mechanical equilibrium, and the reverse argument for  $a$  and  $c$  directions. We remark from the relaxed spatial distribution of the local pressure field that the elastic strain deploys at longer distance from both sides of the electronic HS-LS interface at  $\theta_{\max} = 90^\circ$  in Fig. 6(a) than at  $\theta_{\min} = 130^\circ$  in Fig. 6(b) where the elastic strain is mainly localized around the interface.

In the movie S1 (respectively S2) of Ref. [51], we present the spatiotemporal distribution of the local pressure field through the lattice during the relaxation process at  $\theta_{\max} = 90^\circ$  (respectively  $\theta_{\min} = 130^\circ$ ). We observe the spread of the pressure field inside the lattice: in Fig. 7, we show snapshots from the movie S1 in Fig. 7(a) [respectively S2 in Fig. 7(b)] at different times, representing the growth of the pressure field during the relaxation process. We can notice that there is a phenomenon of propagation and reflection waves, particularly marked in the LS state where for example the compressive strain is propagating from the (left) edge of the lattice toward the HS-LS interface, before reflecting backward on the latter. At the same time, while going backward, the compressive strain extent along the interface, as can be seen for example in Fig. 7(b). Moreover, the establishment of the elastic strain during the relaxation process leads to an antisymmetric distribution of the pressure field around the interface: we show this behavior in Fig. 8, where we display the spatial distribution of the local pressure field through the lattice through the diagonal plane of coordinates  $(\frac{N_x}{2}, \frac{N_y}{2}, z)$  perpendicular to the HS-LS interface and related to Fig. 6 for the relaxed configuration ( $t = 34\,650$  ts) at  $\theta_{\max} = 90^\circ$  and at  $\theta_{\min} = 130^\circ$ .

Furthermore, the intensity of the maximum strain is 25% weaker at  $\theta_{\min} = 130^\circ$  ( $P_{\max} \sim 1500$ ) than at  $\theta_{\max} = 90^\circ$  ( $P_{\max} \sim 2000$ ). Moreover, we observe that the LS (respectively HS) phase is experiencing a positive (respectively

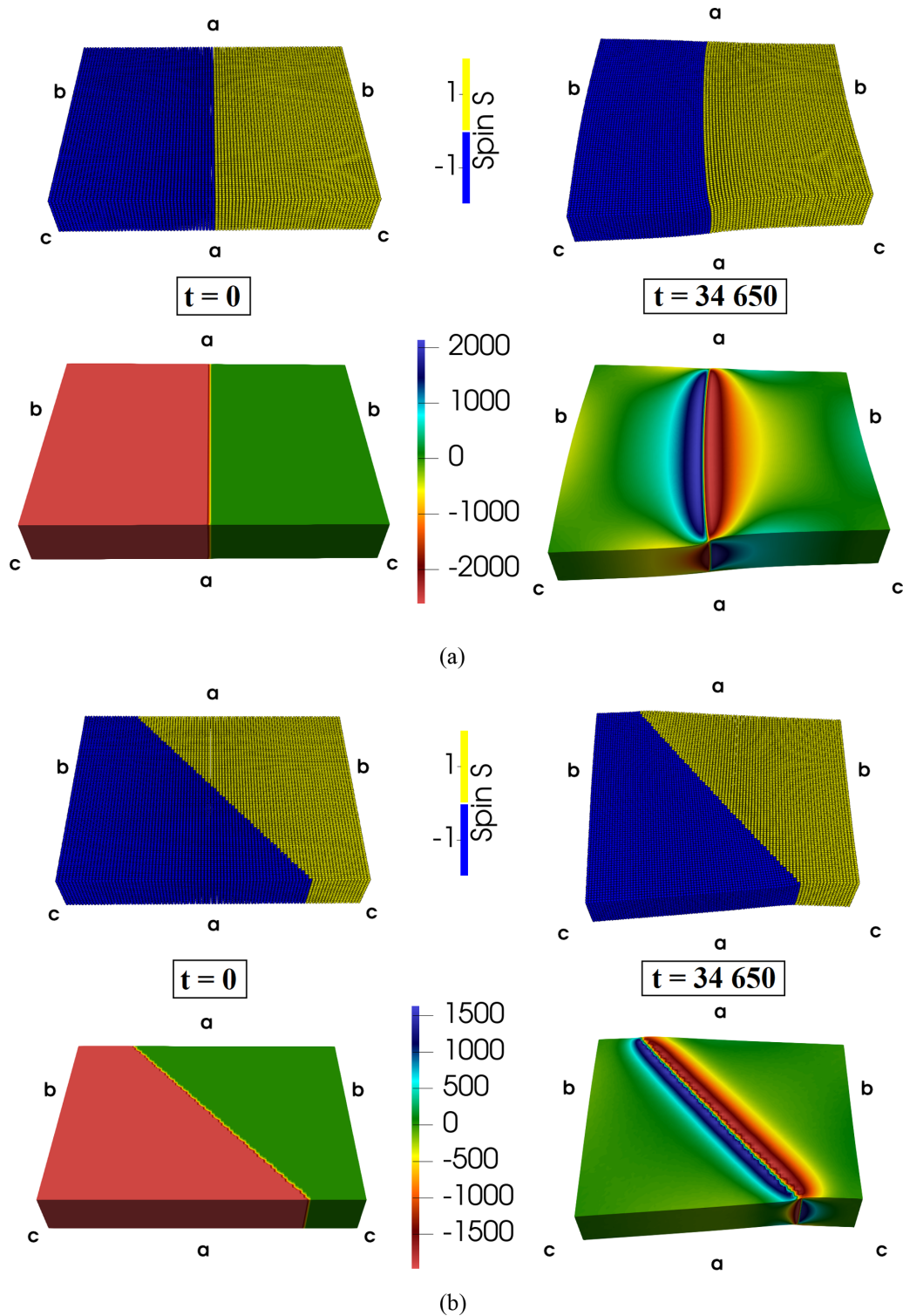


FIG. 6. Spatial configurations of the lattice (top row) and the corresponding distribution of the local pressure field (bottom row), for the initial configuration ( $t = 0$  ts, left column) and the relaxed one ( $t = 34\,650$  ts, right column) for the lattice size  $(96 \times 96 \times 16)$  and  $\lambda = -0.6$ : at (a)  $\theta_{\max} = 90^\circ$  and (b)  $\theta_{\min} = 130^\circ$ . Yellow (blue) spheres represent HS (LS) sites.

negative) pressure close to the interface in the  $(a, b)$  plane, while the situation is reversed in the  $(a, c)$  plane. This is due to the previous arguments of stretching (along  $b$  direction) and contraction (along  $a$  and  $c$  directions). Moreover, we present in Fig. 9 the time dependence of the average local

pressure,  $\langle P \rangle$ , calculated through the whole lattice during the relaxation process for  $\theta_{\min} = 130^\circ$ . Two regimes can be seen in  $\langle P \rangle$  for the whole lattice: (i) a first “explosive” regime between  $t = 0$  and around  $t = 5000$  where the LS phase was under tension, and (ii) a second slower regime between

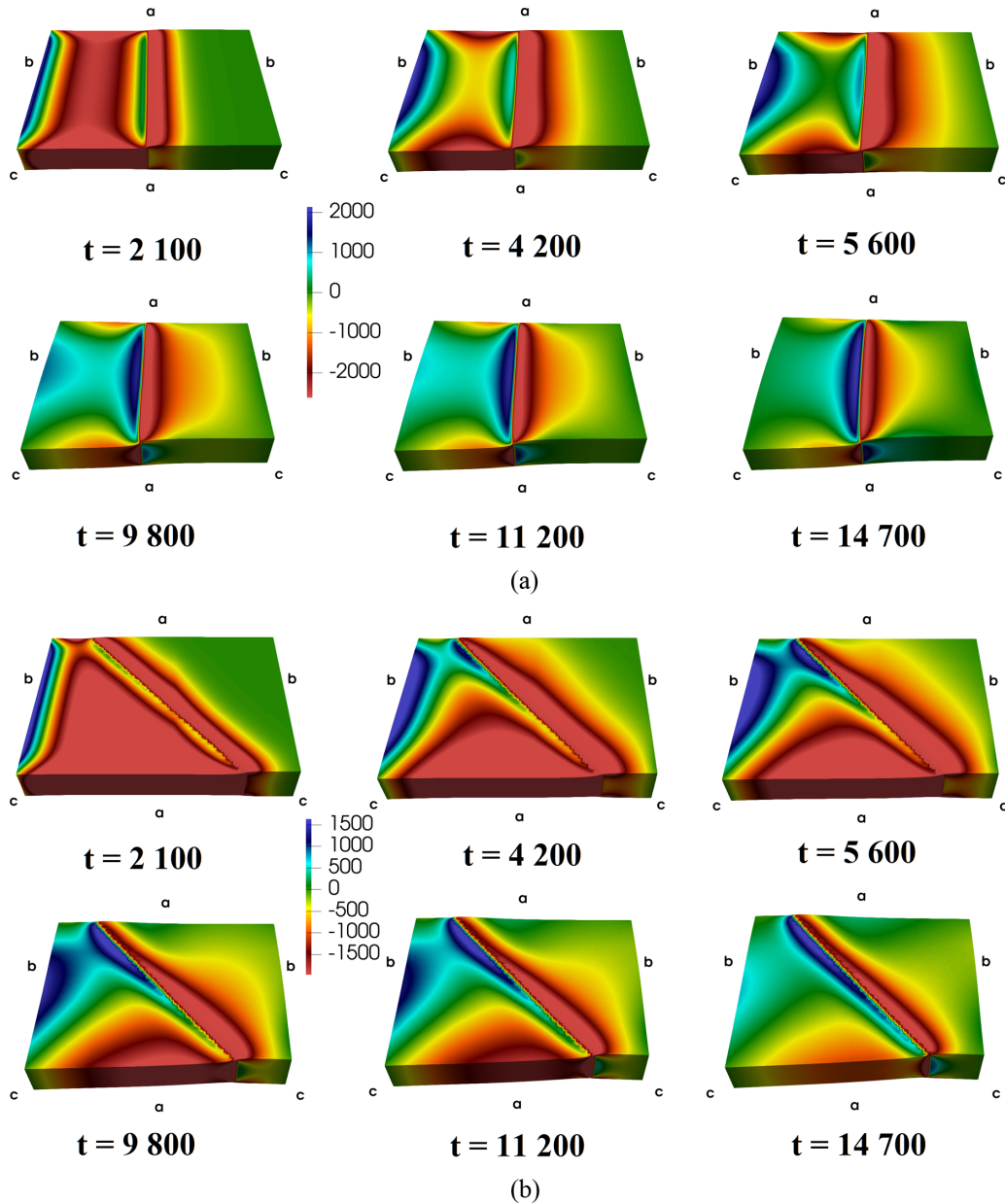


FIG. 7. Spatiotemporal distribution of the local pressure field through the lattice related to Fig. 6, during the relaxation process at different times  $t$  (ts), for the lattice size  $(96 \times 96 \times 16)$  and  $\lambda = -0.6$  at different orientation angles  $\theta_{\min}$ . (a)  $\theta_{\max} = 90^\circ$  and (b)  $\theta_{\min} = 130^\circ$ .

around  $t = 5000$  until the end of the relaxation  $t = 34\,650$  where the change in the pressure occurs essentially in the HS phase, but with a small (about an order of magnitude weaker) variation in the LS phase. In inset, we display the respective contributions,  $\langle P \rangle_{\text{HS}}$  and  $\langle P \rangle_{\text{LS}}$  of the LS and HS phases to the average local pressure field. Here, we see that during the first rapid contraction of the “LS” phase (blue curve), initially prepared with the HS lattice parameter, the HS phase which is supposed to be at equilibrium from the mechanical point of view, is subject to a tension which decreases its average local pressure (yellowish curve) during the 5000 time steps of the simulation. This behavior is interpreted as the reaction of the HS phase to the rapid “crunch” of the LS phase, where the maximum of stress transferred from LS to HS phase is obtained at the minimum of  $\langle P \rangle_{\text{HS}}$ . When the LS lattice enters in the second regime ( $t > 50000$ ) where the relaxation slows

down, the average HS local pressure increases and recovers its initial value,  $\langle P \rangle_{\text{HS}} = 0$ . We conducted similar simulations for the case  $\theta_{\max} = 90^\circ$  for comparison, and the results are summarized in the Figure S1 of [51]. We can observe that there is no significant difference in the global behavior of the latter with respect to the interface’s orientation angle, however we see that (i) for  $\theta_{\min} = 130^\circ$  the contribution of the HS phase to the local pressure field is weaker than for  $\theta_{\max} = 90^\circ$ , and a meticulous inspection shows that (ii) the curve profiles of  $\langle P \rangle_{\text{HS}}$  are very slightly different for the two cases, due to the different spatiotemporal dynamics of the interfaces.

In addition, for  $\theta_{\min} = 130^\circ$ , we remark that the lattice exhibits a bending with a curvature along the  $a$  direction. This implies that the shape of the geometry of the system can adjust itself, thanks to the free boundary conditions, in



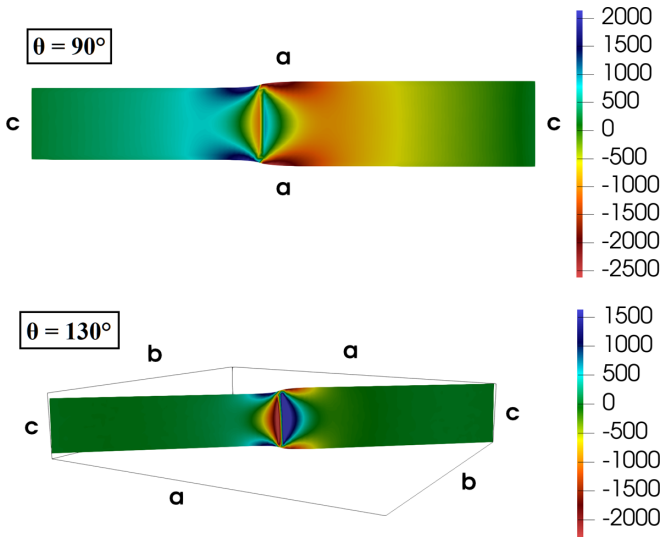


FIG. 8. Spatial distribution of the local pressure field through the lattice in the perpendicular plane of the HS-LS interface located at  $N_x/2$  and  $N_y/2$  and related to Fig. 6, for the relaxed configuration ( $t = 34\,650$  ts), the lattice size ( $96 \times 96 \times 16$ ) and  $\lambda = -0.6$ : at  $\theta_{\max} = 90^\circ$  (top) and  $\theta_{\min} = 130^\circ$  (bottom).

order to reduce the total elastic energy of the lattice. It would be interesting to check if, as in Ref. [38] for 2D systems, the application of a force  $F$  at remarkable points of the simulation lattice here in 3D, could break the symmetry between the two isoenergetic-degenerate minima  $\theta_{\min}$ , and thereby identify the existence of a new bistability in the space parameters  $\theta_{\min}$ - $F$ : this work is left for a next study.

### 3. Energy barrier

We depict in red in Figs. 5(a) and 5(b), where a double well structure appears, the height of the energy barrier  $\Delta E$  ( $K$ ) =  $\langle E(\theta_{\max}) \rangle - \langle E(\theta_{\min}) \rangle$  to overpass in order to switch the inter-

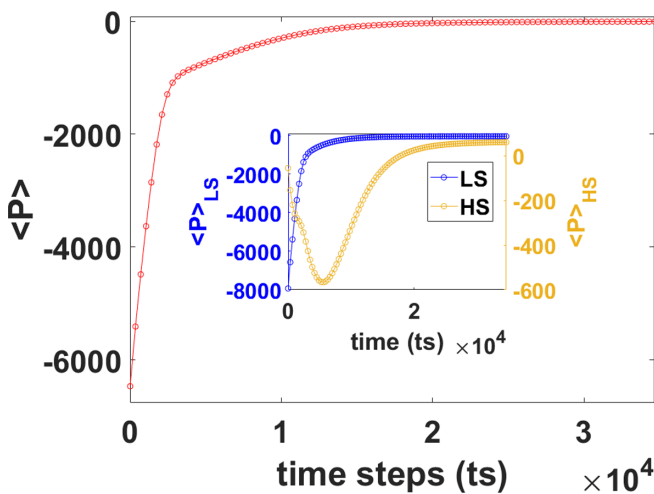


FIG. 9. Average local pressure  $\langle P \rangle$  calculated for the whole lattice as a function of the time  $t$  given in time steps units (ts) during the relaxation process at  $\theta_{\min} = 130^\circ$ , for the lattice size ( $96 \times 96 \times 16$ ) and  $\lambda = -0.6$ . (Inset) Contributions of the LS ( $\langle P \rangle_{\text{LS}}$  in blue) and HS ( $\langle P \rangle_{\text{HS}}$  in yellowish) phase to  $\langle P \rangle$ .

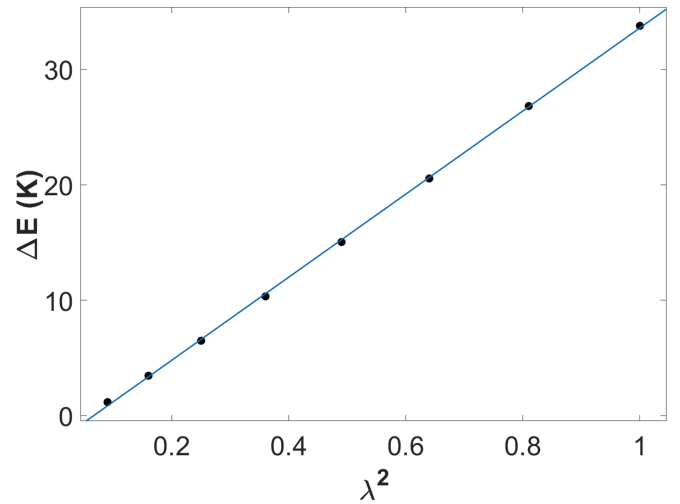


FIG. 10. Height of the energy barrier  $\Delta E$  as a function of the square of the anisotropy ratio parameter  $\lambda$  showing a linear behavior for ( $96 \times 96 \times 16$ ). In blue, we plot a linear regression with 95% confidence bounds.

face orientation from one minimum to the other. This quantity should be of application interest, indicating the energy barrier to overcome to allow experimenter to switch from one minimum to the other isoenergetic one. As one can notice in Figs. 5(a) and 5(b), the height  $\Delta E$  seems to increase with  $|\lambda|$ : from few  $K$  to dozens of  $K$ .

Thus we display in Fig. 10 for the case of ( $96 \times 96 \times 16$ ) the behavior of  $\Delta E$  according to  $\lambda$ , which is a measurable experimental quantity (related to structural/crystallographic data): we realize that the dependence of  $\Delta E$  follows a power law almost parabolic with a positive slope ( $\approx 36$ ). We plot a nonlinear regression with a power law  $\Delta E = f(\lambda^2)$  where a 95% confidence is found. This behavior has been confirmed in all of our tested lattice sizes. This result provides estimation that could be useful for potential applications.

Next, we investigate the size-dependence of  $\Delta E$ , which should be of interest for 3D spin crossover nanoparticles. We show in Fig. 11 the size dependence of  $\Delta E$  for the case of  $\lambda = -0.4$  for “square” shapes ( $N_x \times N_x \times 16$ ) for computational convenience with  $N_x \in [32, 128]$ : a power law can be found. We plot a linear regression using a logarithmic scale on the  $x$  and  $y$  axes, with a power law  $\Delta E \sim (N_x)^\kappa$ , which fits the data with a standard deviation  $R^2 \simeq 0.96$ . A better agreement can be found for the fitting (see Fig. S2 [51]) when using smaller  $\lambda$  values ( $\lambda = -0.6$ ). Indeed, as summarized in Fig. 11(b) displaying  $\lambda$  dependence of  $\kappa$ , one can see that the amplitude of the fluctuations are smaller for large negative  $\lambda$  values, for which the exponent  $\kappa$  seems to reach asymptotically a constant value  $\kappa = (0.25 \pm 0.14)$ .

### 4. Order parameter $\theta_{\min}$ - $\beta$ exponent

From the characteristics of Fig. 5, the behavior of the relaxed elastic energy  $\langle E(\theta_{\min}) \rangle$  is similar to that of the free energy of a second-order phase transition, where the order parameter would be the angle  $\theta_{\min}$  and the control parameter would be the anisotropy ratio  $\lambda$ . We visualize in Fig. 12 the evolution of  $\theta_{\min}$  as a function of  $\lambda$  for the cubic case of

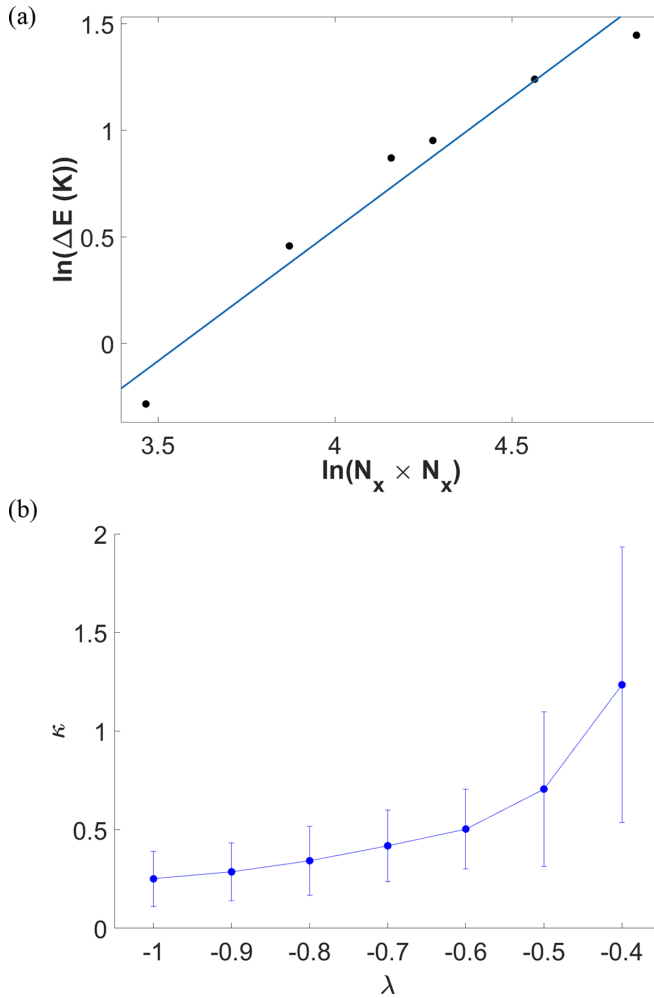


FIG. 11. (a) Size dependence, in a log-log scale, of  $\Delta E(K)$  for the case of  $\lambda = -0.4$  for rectangular shapes ( $N_x \times N_x \times 16$ ) with  $N_x \in [32, 128]$ . (b) Evolution of the  $\kappa$  exponent relative to the anisotropy ratio parameter  $\lambda$ , reaching asymptotically a constant value  $\kappa = 0.25$  for large negative  $\lambda$  values. (a)  $\Delta E$  fits with the linear regression (blue curve) here with a slope  $\kappa \approx 1.235$ , suggesting the power law  $\Delta E \sim (N_x)^\kappa$  for  $\lambda = -0.4$ . (b) Error bars correspond to the confidence bounds (95% level of confidence) for the fitted slopes during the regression of (a) for different values of  $\lambda$ .

( $32 \times 32 \times 32$ ), for computational convenience. This confirms a second-order-like phase transition behavior with the order parameter  $\theta_{\min} \neq 0$  for  $\lambda < \lambda_c = -0.48$  (for this case) and  $\theta_{\min} = 0$  for  $\lambda_c < \lambda < 0$ , with the order parameter remaining “continuous” at the transition. We can see that  $\theta_{\min}$  saturates in the “ordered phase” (below  $\lambda_c$ , at  $14^\circ$  and  $166^\circ$ ), and that in the region from  $\lambda_c$  to 0 only one minimum is present corresponding to the perpendicular interface  $\theta_{\min} = 90^\circ$ . This is interesting because we would naively expect this to happen only in the isotropic case  $\lambda = 1$  as observe previously at 3D [37]. The same kind of results have been obtained for 2D systems [38]. We will come back, later in the paper, on this feature.

In order to study the singular behavior of physical quantities in the vicinity of a second-order phase transition, it is usual to represent them as power laws of a reduced

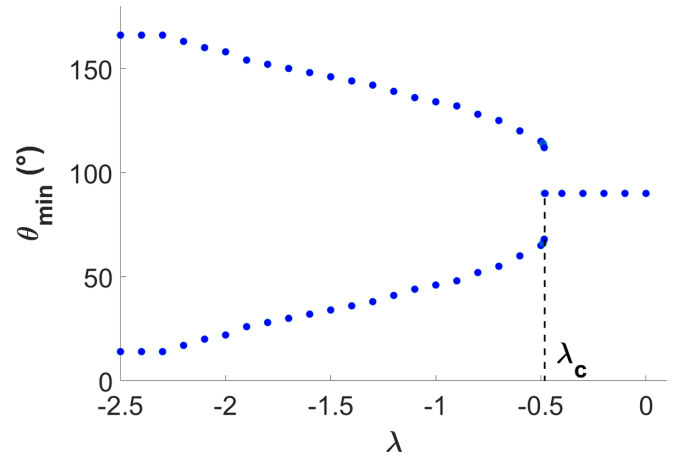


FIG. 12. Evolution of  $\theta_{\min}$  (degrees) as a function of  $\lambda < 0$  for the cubic lattice of size ( $32 \times 32 \times 32$ ).  $\theta_{\min}$  behaves like an order parameter of a second-order phase transition. See text for more explanations.

variable. We note  $\Lambda = (\lambda - \lambda_c)/\lambda_c$  the adimensional reduced anisotropy ratio, measuring the difference in  $\lambda$  with respect to  $\lambda_c$  (distance from the critical point  $\lambda_c$ ). According to this, we are supposed to have  $\theta_{\min} \sim \Lambda^\beta$  with  $\beta$  the critical exponent measuring the strength of the singularity at the critical point  $\lambda_c$ . Subsequently, we will keep only the points of the upper curve of  $\theta_{\min}(\lambda)$  in the “ordered phase” because of the symmetry of the latter around the axis  $\theta_{\min} = 90^\circ$ .

We show in Fig. 13(a) the  $\Lambda$  dependence of  $\theta_{\min}$  for the case of a cubic size ( $64 \times 64 \times 64$ ): a power law can be found. We plot a nonlinear regression using a logarithmic scale on the  $x$  and  $y$  axes, with a power law  $\theta_{\min} \sim \Lambda^\beta$ , confirming this critical behavior. Via Fig. 13(b), we realize that this exponent display a constant value respectively to the size of the system, that is equal to  $\beta = (0.0844 \pm 0.0030)$  by averaging all the data of Fig. 13(b).

Above, we showed the critical exponent  $\beta$  value for cubic sizes of the system only, implicitly guessing that the system undergoes an isotropic phase transition, meaning that only one relevant length scale (the correlation length  $\xi$ ) exists in the vicinity of the phase transition point. To verify if the critical exponent value is size-dependent, we have done the same estimations of  $\beta$  for 37 rectangular system sizes, with  $N_x$  ranging from 16 to 128,  $N_y$  from 16 to 128 and  $N_z$  from 16 to 72. Thereby, in Fig. 14, we exhibit the evolution of  $\beta$  relative to the number of spins ( $N_x \cdot N_y \cdot N_z$ ) inside the lattice, for each of these rectangular system sizes: the number of spins ranges from 4096 to 524 288. We observe that for small system sizes, the exponent values are more spread around the mean value and error bars are wider, which makes sense because for small sizes near the critical point the role of  $\xi$  should be taken by the system size, and this finite value of the correlation length implies that divergences of thermodynamic quantities should be rounded and shifted. On the other hand, for large system sizes the  $\beta$  values are less scattered around the mean and they are found more often into the standard deviation. From this graphic, we found a value of  $\beta = (0.0929 \pm 0.0215)$ , which is consistent with the exponent found for cubic sizes.

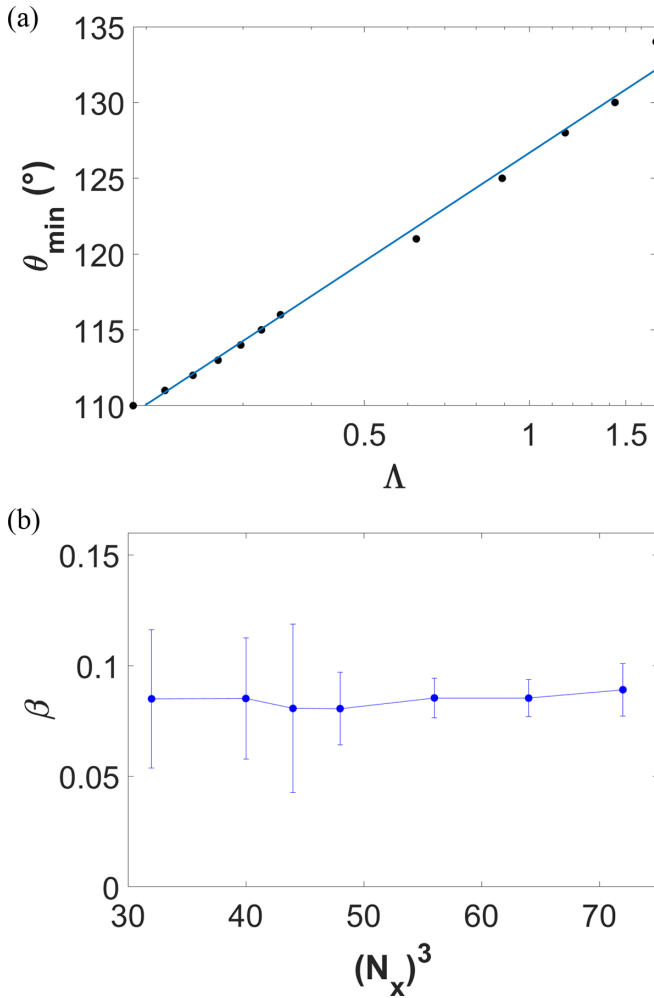


FIG. 13. (a) Evolution of  $\theta_{\min}$  (degrees), in semi-log  $x$  scale, relative to  $\Lambda$  for the case of cubic size ( $64 \times 64 \times 64$ ). (b) Evolution of the  $\beta$  exponent relative to the cubic sizes of the system ( $N_x \times N_x \times N_x$ ) displaying a constant value within the error bars which are significantly lowered for big sizes. (a)  $\theta_{\min}$  fits with the linear regression (blue curve) here with a slope  $\beta = 0.0864 \pm 0.0074$ , suggesting the power law  $\theta_{\min} \sim \Lambda^\beta$ . (b) Error bars correspond to the confidence bounds (95% level of confidence) for the fitted slopes during the regression of (a).

### 5. Correlation length $\xi$ - $\nu$ exponent

A characteristic of a second-order phase transition is the divergence of the correlation length  $\xi$  at the critical value of the control parameter  $\lambda_c = \lambda_c(\infty)$ , where  $\lambda_c(\infty)$  is the critical anisotropy ratio obtained for infinitely large systems (in the thermodynamic limit) where  $L_i = N_i R_0^{HH} \rightarrow \infty$  with  $i = \{x, y, z\}$ .

In the same way as for  $\beta$  exponent, we should have  $\xi \sim \Lambda^{-\nu} \sim (\lambda - \lambda_c(\infty))^{-\nu}$  with  $\nu$  the intrinsic exponent of the correlation length. As previously mentioned, in numerical simulations system size is inevitably finite, and close to  $\lambda_c$  the correlation length is cut-off by the system size. In the rest of the document, we will take the number  $N_i$  instead of the size  $L_i$  because of the straightforward relation between both of them. Thus, by manipulating the previous relations and replacing  $\xi$  by  $N_i$ , we obtain  $\lambda_c(\infty) - \lambda_c(N_i) \sim (N_i)^{-1/\nu}$ ,

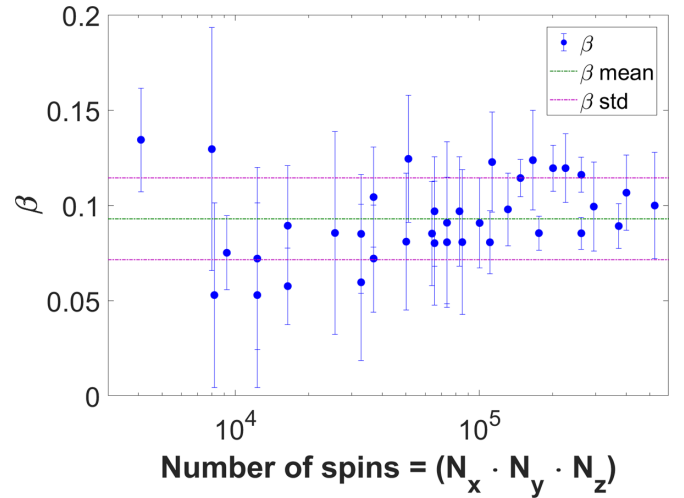


FIG. 14. Evolution of  $\beta$  as a function of the number of spins ( $N_x \times N_y \times N_z$ ) for rectangular system sizes. As before, error bars correspond to the confidence bounds (95% level of confidence) for the fitted slopes of  $\theta_{\min} \sim \Lambda^\beta$  during the regression. The green dashed line represent the mean of these 37 values, while the pink one describe the standard deviation.

where  $\lambda_c(N_i)$  is the anisotropy ratio that is now a function of the size of the system in the relation. Through this relation, we can roughly estimate the value of the  $\nu$  exponent for our simulations. We take only cubic system sizes ( $N_x \times N_x \times N_x$ ), and we measure for each of them the critical point value  $\lambda_c(N_x)$ : we observe that these values increase with  $N_x$  [from  $\lambda_c(N_x = 20) = -0.58$  to  $\lambda_c(N_x = 72) = -0.42$ ], and that  $\lambda_c(N_x)$  values approach asymptotically a constant value for large sizes, that we estimate as  $\lambda_c(\infty) \approx -0.40$ .

As depicted in Fig. 15, we notice that  $\lambda_c(\infty) - \lambda_c(N_x)$  follows a power law: we plot in blue a nonlinear regression using a logarithmic scale on the  $x$  and  $y$  axes, with  $\lambda_c(\infty) - \lambda_c(N_x) \sim (N_x)^{-1/\nu}$ , which gives the value of

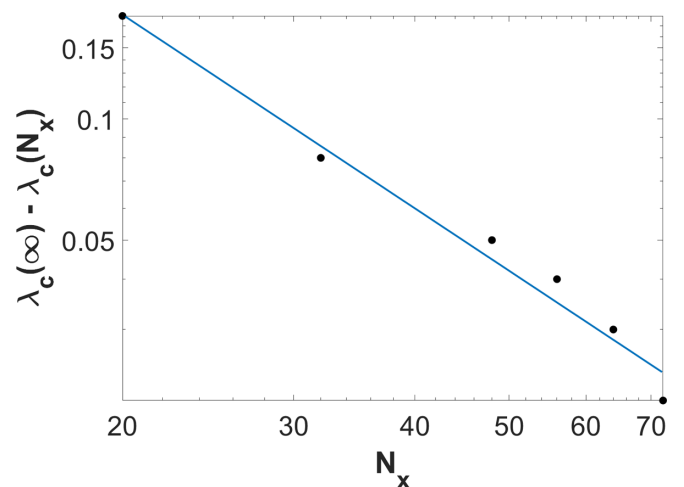


FIG. 15. Evolution of  $\lambda_c(\infty) - \lambda_c(N_i)$ , in log-log scale, relative to  $N_x$  for different cubic sizes ( $N_x \times N_x \times N_x$ ).  $\lambda_c(\infty) - \lambda_c(N_x)$  fits with the linear regression (blue curve) here with a slope  $\nu = 0.63 \pm 0.25$ , suggesting the power law  $\lambda_c(\infty) - \lambda_c(N_x) \sim (N_x)^{-1/\nu}$ .

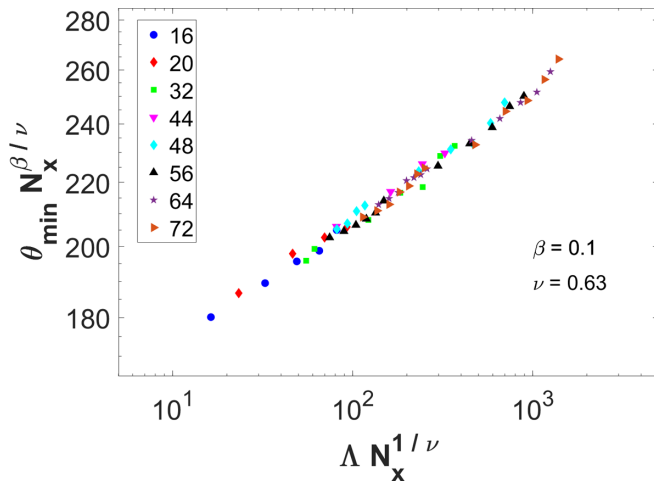


FIG. 16. Evolution of  $\theta_{\min} N_x^{\beta/\nu}$ , in a log-log scale, relative to  $\Lambda N_i^{1/\nu}$  for different cubic sizes ( $N_x \times N_x \times N_x$ ) with  $N_x \in [16, 72]$ . All data collapse on a single curve for  $\beta = 0.1$  and  $\nu = 0.63$ .

$\nu = (0.63 \pm 0.25)$ , with 95% confidence bounds for the fitted slope during the regression.

### 6. Finite size scaling theory

Since phase transitions can only be really observed in the thermodynamic limit, the calculated observables are system-size dependent, and thus quite different from their thermodynamic limit values, especially for small sizes. A finite size scaling (FSS) theory has been developed, thanks to which we can check the critical exponents determined previously. The scaling law connecting the order parameter  $\theta_{\min}$ , the reduced control parameter  $\Lambda$  and the size of the system  $N_i$  is relevant close to the transition and for sufficiently large sizes. Applying the FSS to our case, the scaling form for  $\theta_{\min} \sim \Lambda^\beta$  for finite system with linear size  $N_i$  is given by

$$\theta_{\min}(N_i, \lambda) \sim N_i^{(-\beta/\nu)} \tilde{\theta}(\Lambda N_i^{1/\nu}) \quad (6)$$

The function  $\tilde{\theta}$  is the scaling function of the preferential orientation  $\theta_{\min}$ , and  $\Lambda N_i^{1/\nu}$  is the scaling variable. By inverting Eq. (6), one has  $\theta_{\min}(N_i, \lambda) N_i^{\beta/\nu} \sim \tilde{\theta}(\Lambda N_i^{1/\nu})$ . Figure 16 displays in a log-log scale the plot of the left-hand side of this relation  $\theta_{\min}(N_i, \lambda) N_i^{\beta/\nu}$  as a function of the right one  $\Lambda N_i^{1/\nu}$  for different system sizes. All the points should fall on a single master curve for the correct values of the exponents  $\beta$  and  $\nu$ . On this graphic we have used only cubic system sizes ( $N_x \times N_x \times N_x$ ) from  $N_x = 16$  (4096 spins) to  $N_x = 72$  (373 248 spins), and  $N_i = N_x$  here.

The best data collapse, by the eye, on a single curve is obtained for  $\beta = 0.1$  and  $\nu = 0.63$ . These values are in good agreement with those found above; which tends to confirm that the critical exponent values previously determined are correct. The fact that all data collapse also allows us to confirm that the previous used sizes for our simulations were adequate for the study of the phase transition.

It is interesting to notice that the present values  $\beta = (0.0844 \pm 0.0030)$  and  $\nu = (0.63 \pm 0.25)$ , found for cubic sizes, are consistent with those of the universality class of the four-state  $S = 3/2$  bidimensional Potts model [47,48],

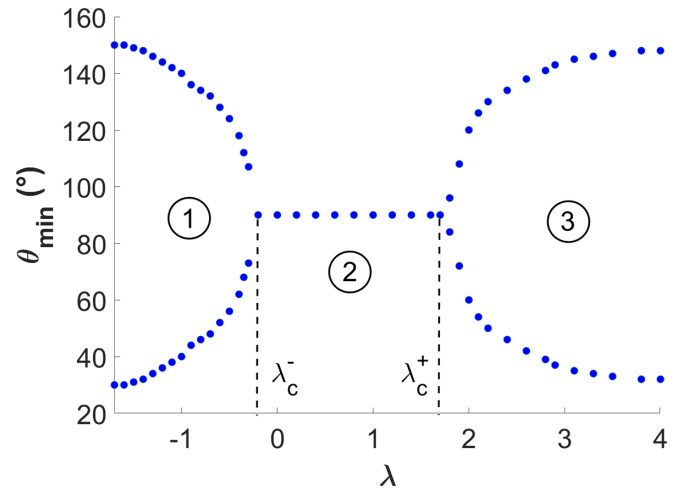


FIG. 17. Evolution of  $\theta_{\min}$  (degrees) as a function of  $\lambda$  for the case of  $(192 \times 48 \times 16)$ :  $\lambda_c^-$  is the critical point of a phase transition for  $\lambda < 0$  values, and  $\lambda_c^+$  is the one for  $\lambda > 0$  values.

where  $\beta = 1/12$  and  $\nu = 2/3$ . In two-dimensional  $q$ -state Potts model, which is a generalization of the Ising model where spins can take more than two values ( $q \geq 2$  values,  $q = 2$  being the case of the Ising model), when  $q \leq 4$ , phase transitions are of second order in the system. Nonetheless, our exponent values don't agree with those of mean field universality class, as it has been found for elastic model of spin-crossover materials ( $\beta = 1/2$  and  $\nu^* = 2/3$  for  $2D$  systems) [49] along the thermally induced transitions. However, the critical exponents determined here correspond to a system with fixed average order parameter (magnetization). In addition, one should notice that the present second-order-like phase transition on the interface orientation is caused by the anisotropic deformation of the unit cell along the spin transition. However, this anisotropy ratio is not a conjugate variable of temperature, as does the isotropic pressure in spin-crossover systems [7,50], which probably complicates the comparison with the critical exponents of the previous studies.

### 7. Stripe bidimensional-like system

Curiously, for stripe bidimensional-like system size we found a peculiar behavior for the preferential orientation  $\theta_{\min}$  of the HS-LS interface. We visualize in Fig. 17 the evolution of  $\theta_{\min}$  as a function of  $\lambda$  for the case of  $(192 \times 48 \times 16)$ , from a negative range of  $\lambda$  values to a positive one.

From Fig. 17, we see that, as previously in our preceding paragraph Sec. III A 4,  $\theta_{\min}$  saturates in the two “ordered phases” [regions (1) and (3), below  $\lambda_c^-$  and above  $\lambda_c^+$  here at  $30^\circ$  and  $150^\circ$ ], while in the region (2) from  $\lambda_c^-$  to  $\lambda_c^+$  only one minimum is present (the perpendicular interface  $\theta_{\min} = 90^\circ$ ). The same results have been obtained for  $2D$  stripe-like system with similar ( $N_x \times N_y$ ) size [38], but for a narrower interval of  $\lambda$  (a width in  $\lambda$  equal to 1 unit in  $2D$  while the width is almost equal to 2 units here in  $3D$ ). This larger window of  $\lambda$ , separating two symmetrical minima, could eventually be of practical interest for experimental designers of switchable molecular solids with respect to the geometry of crystals and

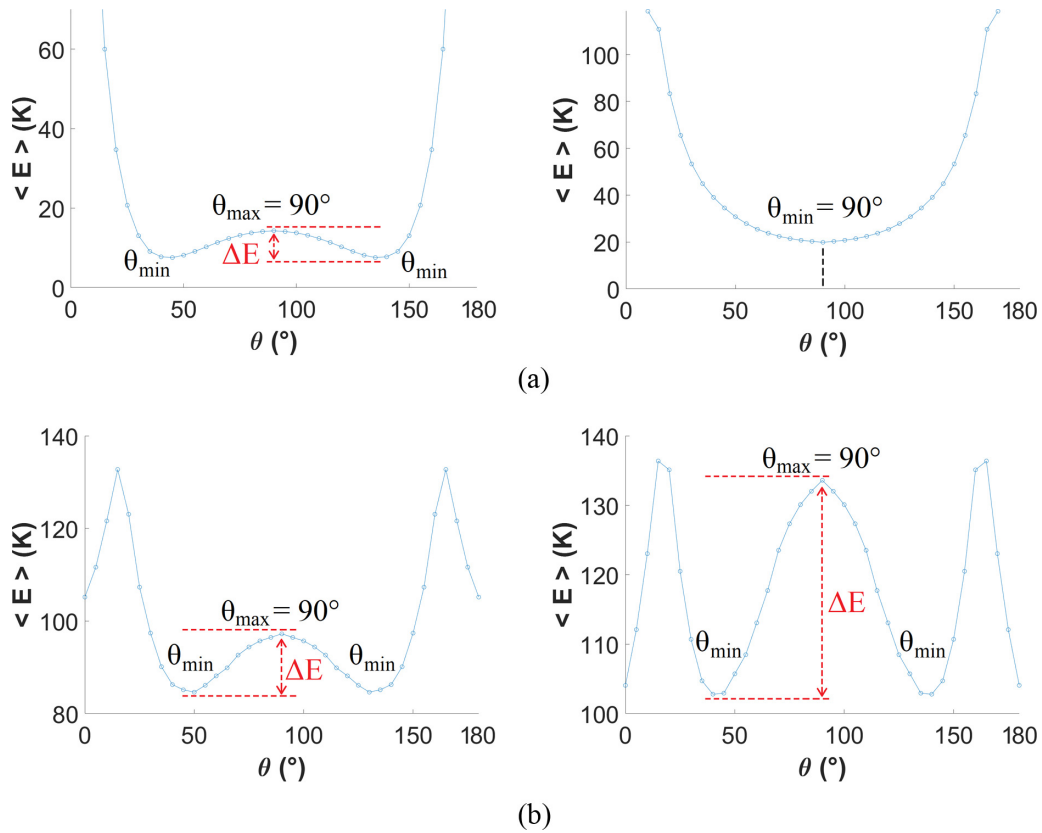


FIG. 18. Energetic landscape  $\langle E \rangle$  (K) as a function of  $\theta$  (degrees) for different anisotropy ratio values  $\lambda$  for a lattice size of  $(192 \times 48 \times 16)$ . In red is represented the height of the energy barrier  $\Delta E$  (K) between peak values  $\theta_{\max}$  and  $\theta_{\min}$  for different  $\lambda$  values. (a)  $\lambda = -1.0$  in region (1); (b)  $\lambda = 1.0$  in region (2); (c)  $\lambda = 2.4$  in region (3); and (d)  $\lambda = 2.8$  in region (3).

the propagation of the HS-LS interface along a direction of space, if wanted to have only a perpendicular interface in the crystal (and not a tilted one).

For  $\lambda < 0$ , we found similar results as in Sec. III A 4, with a second-order phase transition behavior for the order parameter  $\theta_{\min}$  (with  $\beta^- = 0.0819 \pm 0.0262$  here) and  $\theta_{\min} = 90^\circ$  for  $\lambda > \lambda_c^-$  values, with the order parameter remaining “continuous” at the transition. However, beyond a certain value ( $\lambda > \lambda_c^+ = 1.7$ ), we can observe a re-entrant phenomenon for  $\theta_{\min}$  which present again two symmetrical minima.

As depicted in Fig. 18, we display the energetic landscape  $\langle E \rangle$  as a function of  $\theta$ , for lattice size  $(192 \times 48 \times 16)$ , and for different anisotropy ratio values  $\lambda$  taken in the three regions (1)–(3) of Fig. 17. In Fig. 18(a) [and Fig. 18(b)], we display the energetic landscape for  $\lambda = -1.0$  (respectively for  $\lambda = 1.0$ ) which is in the region (1) [respectively in region (2)]: as explained just above, we found the same behavior as in Sec. III A 1 with two symmetrical preferential (stable) orientation  $\theta_{\min}$  and an unstable orientation  $\theta_{\max} = 90^\circ$  in region (1), and only one stable orientation  $\theta_{\min} = 90^\circ$  in region (2). However, in Figs. 18(c) and 18(d), we exhibit the energetic landscape for  $\lambda = 2.4$  (respectively for  $\lambda = 2.8$ ) which are both in the region (3). We observe the re-entrant phenomenon for  $\theta_{\min}$  which present again two symmetrical minima  $\theta_{\min}$  and a unstable orientation  $\theta_{\max} = 90^\circ$ .

Analysing this re-entrant phenomenon as a phase transition too, with  $\theta_{\min} \sim (\Lambda^\dagger)^{\beta^\dagger}$  where  $\Lambda^\dagger = (\lambda - \lambda_c^+)/\lambda_c^+$ , we find

that  $\beta^\dagger = 0.14 \pm 0.02$ , which could naively be compared to the 2D Ising model (where  $\beta = 1/8$ ). Nonetheless, further investigations have to be done in stripe bidimensional-like system sizes to confirm those results, and thus to really compare with other universality classes, this work is left for later.

Moreover, during this re-entrant phenomenon (above  $\lambda_c^+$ ), the height of the energy barrier  $\Delta E$  relative to the anisotropy ratio  $\lambda$  behaves in the same way as the energy barrier for the case  $\lambda < 0$ . We exhibit this behavior in Fig. 19:  $\Delta E$  follows also here a power law almost parabolic with a positive slope ( $\approx 9$ ), as indicated by the nonlinear regression  $\Delta E = f(\lambda^2)$  for which a 95% confidence is found. This parabolic compartment reinforce our hypothesis of a common behavior of the height of the energy barrier between peak values.

We show in Fig. 20 the spatial configurations and the corresponding spatial distribution of the local pressure field, for the initial configuration ( $t = 0$ ) and the relaxed one ( $t = 95\,000$  ts), for the lattice size  $(192 \times 48 \times 16)$  for  $\lambda = 2.4$  [region (3) of Fig. 17] at  $\theta_{\max} = 90^\circ$  in Fig. 20(a) and at  $\theta_{\min} = 130^\circ$  in Fig. 20(b).

We see from the two relaxed spatial configurations of Fig. 20 that the sublattice of the LS state phase contracts anisotropically along the  $b$ ,  $a$  and  $c$  directions with a stronger contraction along the  $b$  direction relative to the two others directions, as expected by the same considerations as in the paragraph Sec. III A 2. Indeed, since the whole lattice was initially set with all of the  $1n$  equilibrium distances equal

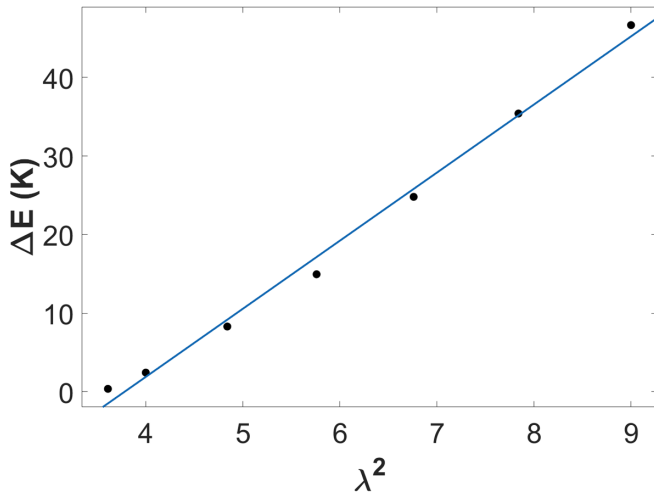


FIG. 19. Height of the energy barrier  $\Delta E$  (K) for the re-entrant phenomenon [region (3) of Fig. 17] as a function of the square of the anisotropy ratio parameter  $\lambda$  showing a linear behavior for  $(192 \times 48 \times 16)$ . In blue, we plot a linear regression with 95% confidence bounds.

to those of the HS state, this imposes the sublattice of the LS state phase to reach its equilibrium position during the relaxation process. Because  $\Delta a > 0$  and  $\Delta c > 0$ , then  $\lambda > 0$  imply  $\Delta b > 0$  meaning that  $b_{HH} > b_{LL}$ , corresponding to a contraction along the  $b$  direction in the mechanical equilibrium, and the similar argument for  $a$  and  $c$  directions.

Through the spatial distribution of the local pressure field for relaxed configurations, we notice that the elastic strain deploys at longer distance from both sides of the electronic HS-LS interface at  $\theta_{\max} = 90^\circ$  [in Fig. 20(a)] than at  $\theta_{\min} = 130^\circ$  [in Fig. 20(b)] where the elastic strain is narrower around the interface. However, we note that at  $\theta_{\max} = 90^\circ$ , despite the spread of the elastic strain from both side of the interface, the local pressure field intensity is weaker than at  $\theta_{\min} = 130^\circ$ , where even if the elastic strain is spatially restricted around the interface, the compressive (tensile) strain is almost multiplied by a factor 2.

## B. Anisotropy ratio $\lambda > 0$

Now, we study the case of anisotropy  $\lambda = \Delta b / \Delta a > 0$  where the unit cell stretches anisotropically along the three directions (slower expansion along the  $b$  direction relative to the  $a$  and  $c$  directions for  $0 < \lambda < 1$ , and stronger expansion along the  $b$  direction relative to the two others directions for  $\lambda > 1$ ) along the LS to HS transition. As a remainder, isotropic case is defined by  $\lambda = 1$ .

### 1. Energy angular dependency

Following the same procedure as in Sec. III A 1 for  $\lambda < 0$ , we look for the preferential orientation for the HS-LS interface, and calculate the energetic landscape  $\langle E \rangle$  relative to  $\theta$  for different anisotropy ratio rates  $\lambda > 0$ , as shown in Fig. 21 for the lattice size  $(96 \times 96 \times 16)$  and  $\theta \in [0^\circ, 180^\circ]$ . The landscape presented here is representative of what we obtain for our few tested lattice sizes in this region of  $\lambda$  compare to the  $\lambda < 0$  situation. We should point out that we

found the same energetic behavior for another bidimensional-like size  $(32 \times 32 \times 16)$ , as well as for cubic lattices such as  $(32 \times 32 \times 32)$  or  $(56 \times 56 \times 56)$ .

In the interval from  $\lambda = 0.3$  to  $\lambda = 0.6$  [Figs. 21(a) and 21(b)],  $\langle E(\theta) \rangle$  shows a single minimum at  $\theta_{\min} = 90^\circ$ , corresponding to the interface in the  $(b, c)$  plane.

Increasing  $\lambda$  [Figs. 21(c), 21(d), and 21(e)] from  $\lambda = 0.9$  to  $\lambda = 1.1$ , two symmetrical maxima  $\theta_{\max}$  appear between  $90^\circ$  and the edges of the angular interval.  $\theta_{\min} = 90^\circ$  is still the preferential orientation, and the HS-LS interface is stuck in this orientation because of the large energy barrier  $\Delta E$  (K) =  $\langle E(\theta_{\max}) \rangle - \langle E(\theta_{\min}) \rangle$  between peak values  $\theta_{\max}$  and  $\theta_{\min}$ . We remark that the  $\theta_{\min} = 90^\circ$  minima rises in energy when  $\lambda$  increases, and then the energy barrier  $\Delta E$  (K) decreases: from  $\Delta E$  (K)  $\approx 22$  K for  $\lambda = 0.9$  to  $\Delta E$  (K)  $\approx 14$  K for  $\lambda = 1.1$ . This behavior lasts until  $\lambda = 1.7$  where the energy barrier vanishes. In addition, we remark that the total elastic energy of the system increases at  $\theta_{\max}$  with  $\lambda$ , from  $\langle E(\theta_{\max}) \rangle \approx 72$  K for  $\lambda = 0.9$  to  $\langle E(\theta_{\max}) \rangle \approx 86$  K for  $\lambda = 1.1$ .

Beyond  $\lambda > 1.7$  [Fig. 21(f) where  $\lambda = 2.0$ ],  $\theta_{\max} = 90^\circ$  become a maximum, and so an unstable position for the interface, where the total elastic energy comes to  $\langle E(\theta_{\max}) \rangle \approx 220$  K.

This is interesting because it means that the perpendicular orientation that have been see previously in the thermal isotropic 3D case [37] stays the preferential orientational response from the system to the HS-LS transition for “moderate” positive  $\lambda$  values. However, for large positive  $\lambda$  value ( $> 1.7$ ), the perpendicular orientation turn to be unstable and it is energetically better for the lattice to have tilted (non perpendicular) interface during the HS-LS transition.

### 2. Relaxed spatial configurations and local pressure field

We show in Fig. 22 the spatial configurations of the lattice, and the corresponding distribution of the local pressure field of the lattice, for different positive  $\lambda$  values for the relaxed configuration ( $t = 33\,250$  ts) at  $\theta = 90^\circ$  and the lattice size  $(96 \times 96 \times 16)$ .

As can be seen in Fig. 22(a), the sublattice of the LS state phase contracts anisotropically along the  $b$ ,  $a$  and  $c$  directions (with a stronger contraction along the  $b$  direction relative to the two others directions when  $\lambda > 1$ ), as expected by the same considerations as in the paragraph Sec. III A 7.

Through the spatial distribution of the local pressure field in Fig. 22(b), we notice that the elastic strain deploys at longer distance from both sides of the electronic HS-LS interface for large positive  $\lambda$  values than for smaller ones where the elastic strain is narrower around the interface. We observe for small values of  $\lambda$  that the LS (respectively HS) phase is experiencing a positive (respectively negative) pressure close to the interface in the  $(a, b)$  plane, while the situation is reversed in the  $(a, c)$  plane. Whereas, for large values of  $\lambda$ , the situation is reversed with the LS (respectively HS) phase experiencing a negative (respectively positive) pressure close to the interface in the  $(a, b)$  plane, and inversely in the  $(a, c)$  plane. Moreover, for small values of anisotropy ratio (e.g.,  $\lambda = 0.3$ ) the local pressure field intensity is weaker than for large values (e.g.,  $\lambda = 2.0$ ): the compressive (tensile) strain is multiplied by a factor 2 (2.5).

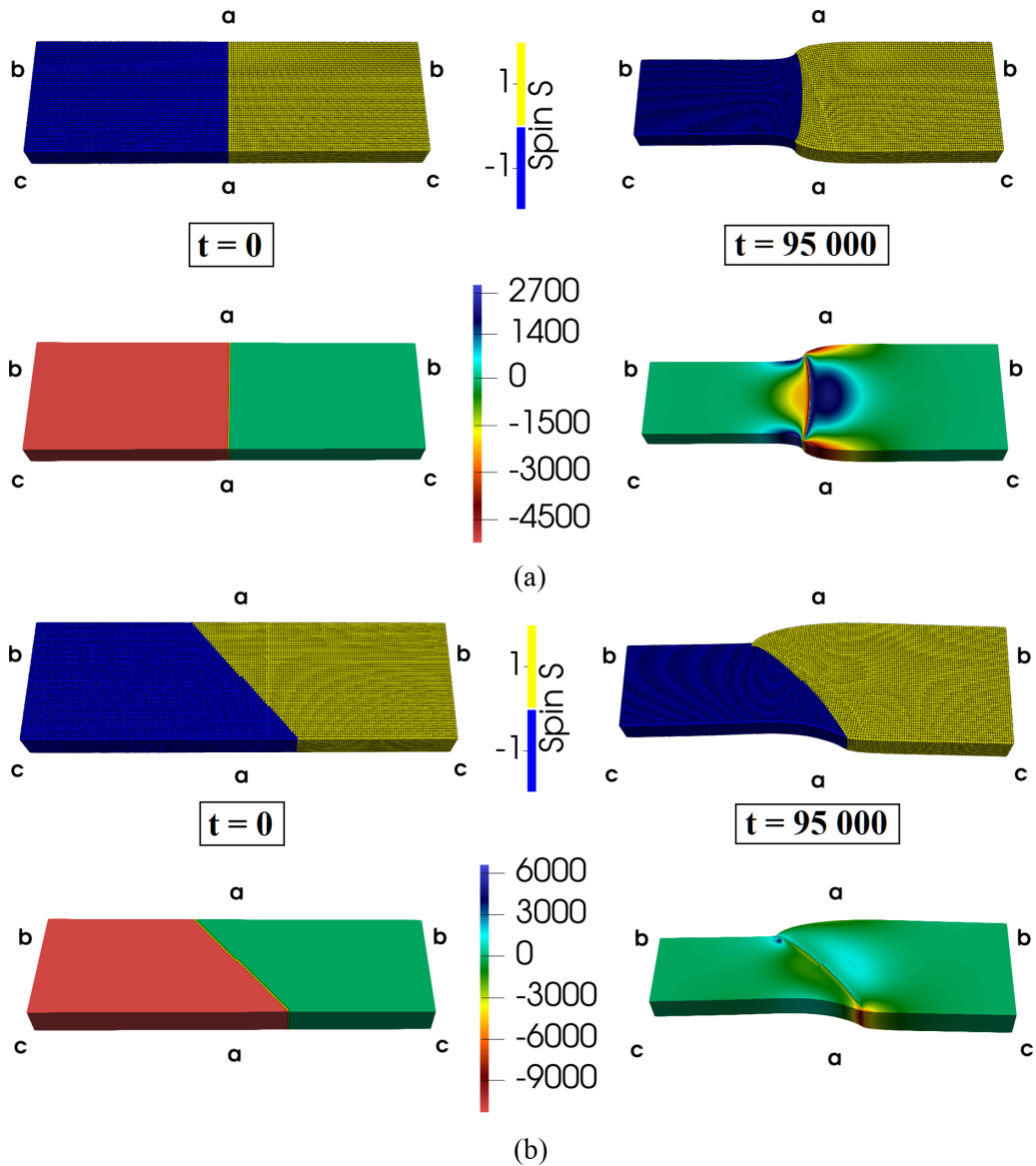


FIG. 20. Spatial configurations of the lattice (top row) and the corresponding distribution of the local pressure field (bottom row), for the initial configuration ( $t = 0$  ts, left column) and the relaxed one ( $t = 95\,000$  ts, right column) for the lattice size ( $192 \times 48 \times 16$ ) and  $\lambda = 2.4$ : (a) at  $\theta_{\max} = 90^\circ$  and (b) at  $\theta_{\min} = 130^\circ$ . Yellow (blue) spheres represent HS (LS) sites. (a)  $\theta_{\max} = 90^\circ$  and (b)  $\theta_{\min} = 130^\circ$ .

These results (Fig. 22) are consistent with the fact that  $\theta = 90^\circ$  goes from minimum to maximum, and so from stable to unstable orientation of the interface, while  $\lambda$  increases in positive values.

We display in Fig. 23 the spatial configurations of the lattice and the corresponding distribution of the local pressure field, for the relaxed configuration ( $t = 33\,250$  ts) at  $\theta_{\max}$  and the simulation size ( $96 \times 96 \times 16$ ), for different positive  $\lambda$  values where a minimum  $\theta_{\min} = 90^\circ$  and two symmetrical maxima  $\theta_{\max}$  coexist in the energetic landscape. We choose to display only the maximum  $\theta_{\max} > 90^\circ$  for easiness because of the symmetry of the energetic landscape.

From the spatial configurations of the lattice of Fig. 23, we remark for all  $\lambda$  values the presence of an additional bending along the  $b$  direction, coexisting with the previously obtained one along the  $a$  direction, discussed in Sec. III A 1. The lattice is more distorted in the case of positive  $\lambda$  values

than in negative values, where we saw previously an abrupt bending along the  $a$  direction (more like a “fracture” along this direction) in Fig. 6(b), however for positive values the lattice is here smoother deformed. This behavior could give insights about the resilience of experimental crystals, upon repeated switching, with regard to the anisotropy ratio rate  $\lambda$ .

From spatial distribution of the local pressure field of the lattice in Fig. 23, we can notice that the elastic strain deploys here too from both sides of the electronic HS-LS interface, however the maximal strain (compressive or tensile) is localized in the nearby of the interface. In addition, for  $\lambda = 1.0$  the isotropic case, the strain scale has a smaller range than for  $0 < \lambda < 1$  or  $\lambda > 1$ .

Besides, we present in Fig. 24 the spatial distribution of the local elastic energy field through the lattice for the relaxed configuration ( $t = 33\,250$  ts) and the simulation size ( $96 \times 96 \times 16$ ) at  $\theta_{\min} = 90^\circ$  and at  $\theta_{\max}$ , for different  $\lambda$  values.

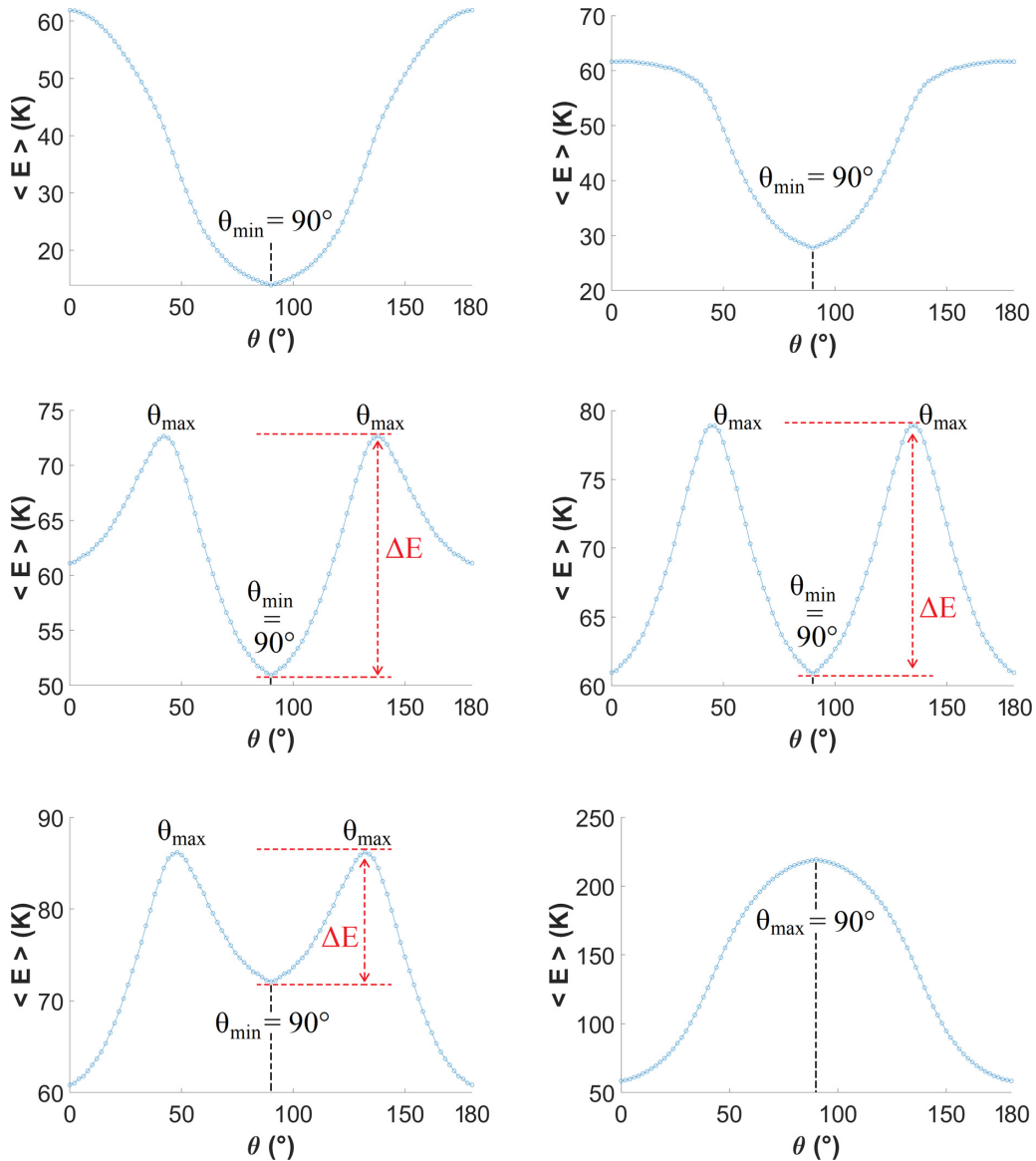


FIG. 21. Energetic landscape  $\langle E \rangle$  (K) as a function of  $\theta$  (degrees) for different anisotropy ratio values  $\lambda > 0$  for a lattice size of  $(96 \times 96 \times 16)$ . We note  $\theta_{\max}$  maxima and  $\theta_{\min}$  minima. In red is represented the height of the energy barrier  $\Delta E$  (K) between peak values  $\theta_{\max}$  and  $\theta_{\min}$  for different  $\lambda$  values. (a)  $\lambda = 0.3$ , (b)  $0.6$ , (c)  $0.9$ , (d)  $1.0$ , (e)  $1.1$ , and (f)  $\lambda = 2.0$ .

We realize that the elastic energy is mainly stored around the HS-LS interface, whatever the angle  $\theta$  is. However, at  $\theta_{\min} = 90^\circ$ , the elastic energy stored increases with the  $\lambda$  value, while the elastic energy stored around the interface exhibits a minimum for the isotropic case  $\lambda = 1.0$  at  $\theta_{\max}$  (with a maximum value of the elastic energy field  $\approx 750$  K for  $0 < \lambda < 1$  and for  $\lambda > 1$ , but a maximum value of the field  $\approx 650$  K for  $\lambda = 1.0$ ).

Therefore the isotropic case  $\lambda = 1.0$  is more favorable for the system than when anisotropy is introduced in the lattice with  $0 < \lambda < 1$  or  $\lambda > 1$ .

### 3. Energy barrier

Furthermore, the height of the energy barrier  $\Delta E$  (K) =  $\langle E(\theta_{\max}) \rangle - \langle E(90^\circ) \rangle$ , relative to the anisotropy ratio  $\lambda$  behaves quite well as the energy barrier for the case  $\lambda < 0$  (see Fig. 10). In Fig. 25, we plot a nonlinear regression with a

power law  $\Delta E = f(\lambda^2)$  where a 95% confidence is found.  $\Delta E$  follows here a power law almost parabolic but with a negative slope ( $\approx -20$ ), whereas for the case  $\lambda < 0$  it was parabolic with a positive slope.

This negative slope is due to the fact that  $\theta = 90^\circ$  is a maximum for large negative  $\lambda$  values, while it becomes a maximum for large positive  $\lambda$  values. The behavior of the energy barrier between peak values for this anisotropy region is similar to the  $\lambda < 0$  region, leaving open the possibility of a common behavior of the height of the energy barrier with respect to  $\lambda$ , no matter what kind of anisotropy is introduced in the system.

### 4. Order parameter $\theta_{\max}$ - $\beta^+$ exponent

We realize that the symmetrical maxima  $\theta_{\max}$  in Figs. 21(c), 21(d), and 21(e) tend toward  $\theta_{\max} = 90^\circ$  while increasing  $\lambda$ .



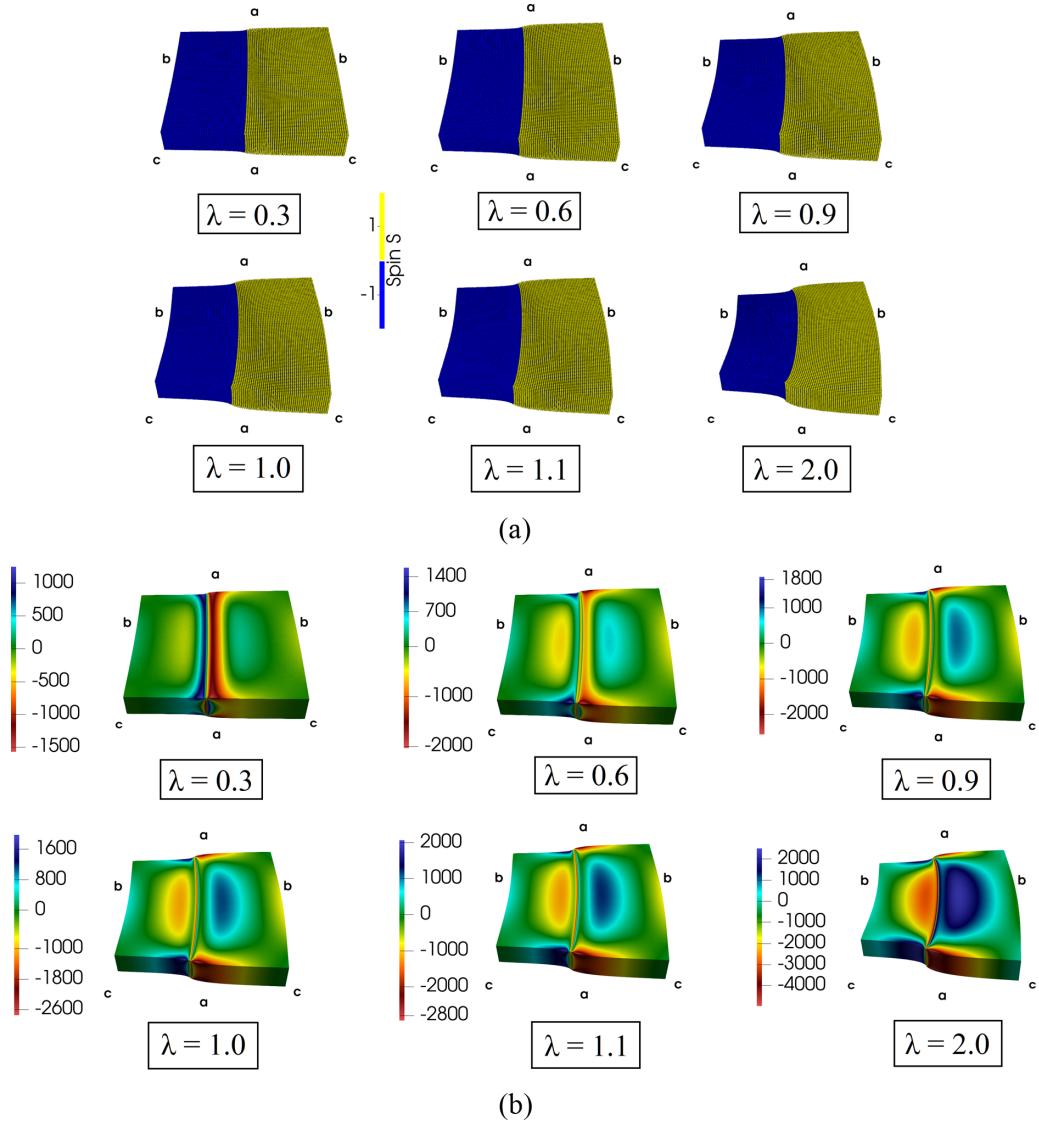


FIG. 22. For the relaxed configuration ( $t = 33\,250$  ts) at  $\theta = 90^\circ$  and the lattice size ( $96 \times 96 \times 16$ ): (a) selected spatial configurations of the lattice - yellow (blue) spheres represent HS (LS) sites, and (b) corresponding distribution of the local pressure field, for different  $\lambda$  values. (a) Spatial configurations of the lattice at  $\theta = 90^\circ$  for different  $\lambda$  values. (b) Spatial distribution of the local pressure field of the lattice at  $\theta = 90^\circ$  for different  $\lambda$  values.

As previously done, for computational convenience, we show in Fig. 26(a) the evolution of  $\theta_{\max}$  relative to  $\lambda$  for the cubic lattice ( $32 \times 32 \times 32$ ), always implicitly guessing that the system undergoes an isotropic phase transition, and thus we choose a cubic lattice where previous results showed that they were size-independent. We remark that it behaves like a second-order phase transition with a critical point at  $\lambda_c^+ = 1.7$ . It is noteworthy that  $\lambda = 1.7$  is equal to the value of the critical point for the phase transition of  $\theta_{\max}$  found in Secs. III A 7 and III B 1.

Taking the same assumptions as before, we suppose it should behave as  $\theta_{\max} \sim (\Lambda^+)^{\beta^+}$  with  $\theta_{\max}$  the order parameter and  $\Lambda^+ = |(\lambda - \lambda_c^+)/\lambda_c^+|$  the reduced anisotropy ratio.

We display, in a semilogarithmic  $x$  scale, in Fig. 26(b),  $\theta_{\max}$  as a function of  $\Lambda^+$ : we plot a nonlinear regression (in blue) with a power law  $\theta_{\max} \sim (\Lambda^+)^{\beta^+}$ , which fits quite good the data with  $\beta^+ = 0.082 \pm 0.018$ . To ensure that these data are

size-independent, we perform the same procedure to a larger cubic size ( $56 \times 56 \times 56$ ) and we find  $\beta^+ = 0.088 \pm 0.010$ . This  $\beta^+$  exponent is in good agreement with the  $\beta$  critical exponent determined for the order parameter  $\theta_{\min}$  in the region of anisotropy ratio  $\lambda < 0$ , in Sec. III A 4. It would suggest that the two phase transitions,  $\theta_{\min}$  for anisotropy ratio  $\lambda < 0$  and  $\theta_{\max}$  for  $\lambda > 0$ , fall in the same universality class.

#### IV. CONCLUSION

In conclusion, SCO materials are among the most fascinating molecular-based solids displaying spectacular reversible first-order solid to solid phase transitions accompanied with the switching of several physical and chemical properties, affecting their electronic, elastic, magnetic, optical and vibrational responses. These transitions can be controlled by several external stimuli, such as temperature, electric field,

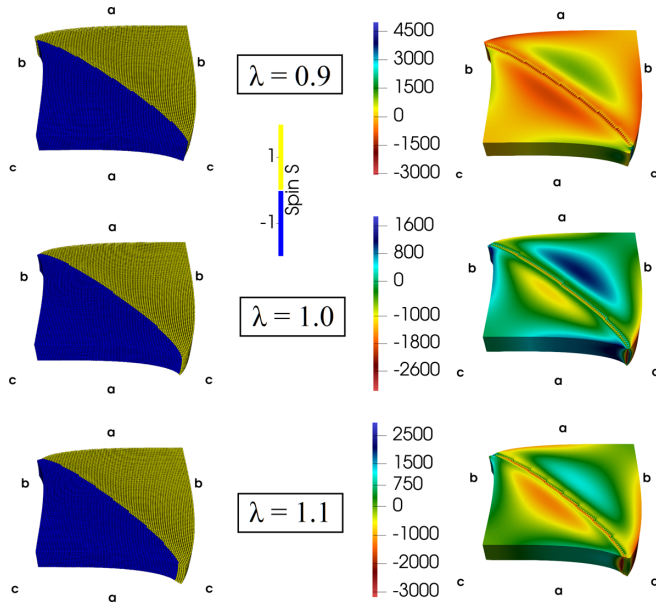


FIG. 23. Spatial configurations of the lattice (left column) and the corresponding distribution of the local pressure field (right column) for the relaxed configuration ( $t = 33\,250$  ts) and the simulation size ( $96 \times 96 \times 16$ ) at (top)  $\theta_{\max} = 138^\circ$  for  $\lambda = 0.9$ , (middle)  $\theta_{\max} = 134^\circ$  for  $\lambda = 1.0$ , (bottom)  $\theta_{\max} = 132^\circ$  for  $\lambda = 1.1$ . Yellow (blue) spheres represent HS (LS) sites.

light, magnetic field, pressure, etc. Despite of their exciting properties opening the way for their integration in future devices for molecular electronics or as displays, or a new generation of sensors, these materials suffer from a several drawbacks when used as single crystals. The most serious one relates to their fragile character which causes their deterioration at the transition, due to the significant volume change between the LS and the HS states leading in most

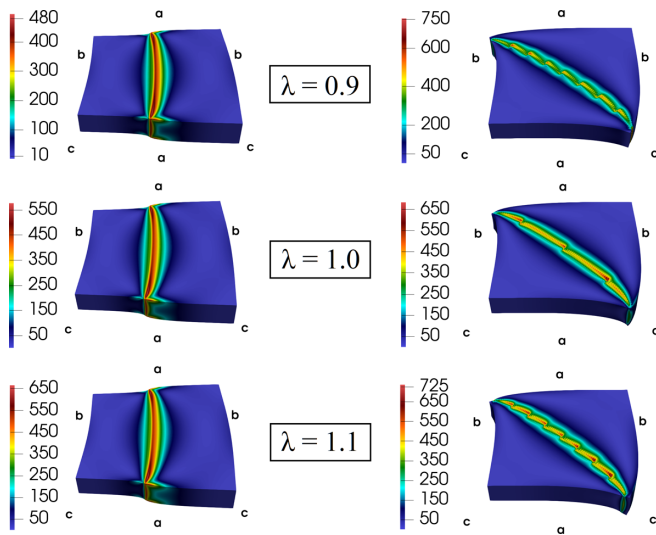


FIG. 24. Spatial distribution of the local elastic energy field of the lattice for the relaxed configuration ( $t = 33\,250$  ts) and the simulation size ( $96 \times 96 \times 16$ ) at  $\theta_{\min} = 90^\circ$  (left column) and at  $\theta_{\max}$  (right column), for (top)  $\lambda = 0.9$ , (middle) 1.0, and (bottom) 1.1.

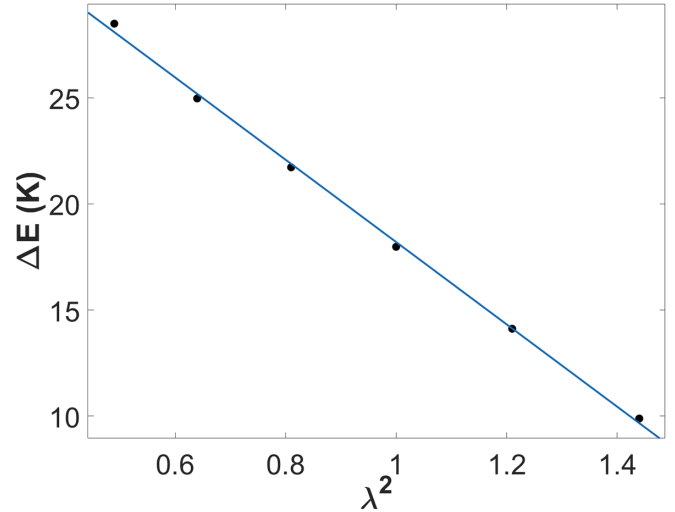


FIG. 25. Height of the energy barrier  $\Delta E$  (K) =  $\langle E(\theta_{\max}) \rangle - \langle E(90^\circ) \rangle$  as a function of the square of the anisotropy ratio parameter  $\lambda$  showing a linear behavior for ( $96 \times 96 \times 16$ ). In blue, we plot a linear regression with 95% confidence bounds.

of the cases to the accumulation of high elastic stress along their transformation. A hope is born with the observation of few exceptions showing SCO single crystals undergoing several thermal cycles keeping their integrity and their physical properties. These systems, showed tilted interfaces having two preferential orientations that emerge spontaneously in the experiments. The aim of the present work is to demonstrate that: (i) the tilting of the interface has a microscopic structural origin and is related to the change of the unit cell between the LS and HS states on the one hand, (ii) and on the other, this orientation results from the optimization of the elastic energy related to lattice misfit and allows to minimize the elastic strain in the lattice which helps to keep the integrity of the crystals.

We have confirmed in this work that anisotropic structural transformations are among the physical reasons at the origin of the emergence of preferential front interface orientations, leading to resilient SCO crystals along the solid to solid LS to HS phase transformations. We have developed an anisotropic version of 3D electroelastic model describing SCO transition, including both spin and volume change during the conversion between the LS and the HS states. In this work, we considered parallelepipedic 3D constituted of unit cells with lattice parameters,  $a$ ,  $b$ ,  $c$ , in the three space directions. During the transition from LS to HS, the unit cell parameters change by  $\Delta a$ ,  $\Delta b$ , and  $\Delta c$ , where we set  $\Delta a = \Delta c$  and use the anisotropy ratio,  $\lambda = \Delta b / \Delta a$ , as a control parameter. We have examined separately the two possible situations of anisotropy where  $\lambda < 0$  or  $\lambda > 0$ , while the isotropic case is defined by  $\lambda = 1$ .

For  $\lambda < 0$ , the unit cell contracts along the  $y$  direction and stretches along the  $x$  and  $z$  directions along the LS to HS transition. The analysis of the relaxed total elastic energy,  $E_{\text{elas}}$  with respect to the interface tilting,  $\theta$ , revealed that the quantity,  $(\theta_{\min} - 90^\circ)$  (where  $\theta_{\min}$  is the preferential orientation) behaves like a second-order phase transition with  $\lambda$ . Moreover, the height of the energy barrier  $\Delta E(K)$  between extrema  $\theta_{\min}$  and  $\theta_{\max} = 90^\circ$  has been found to follow a

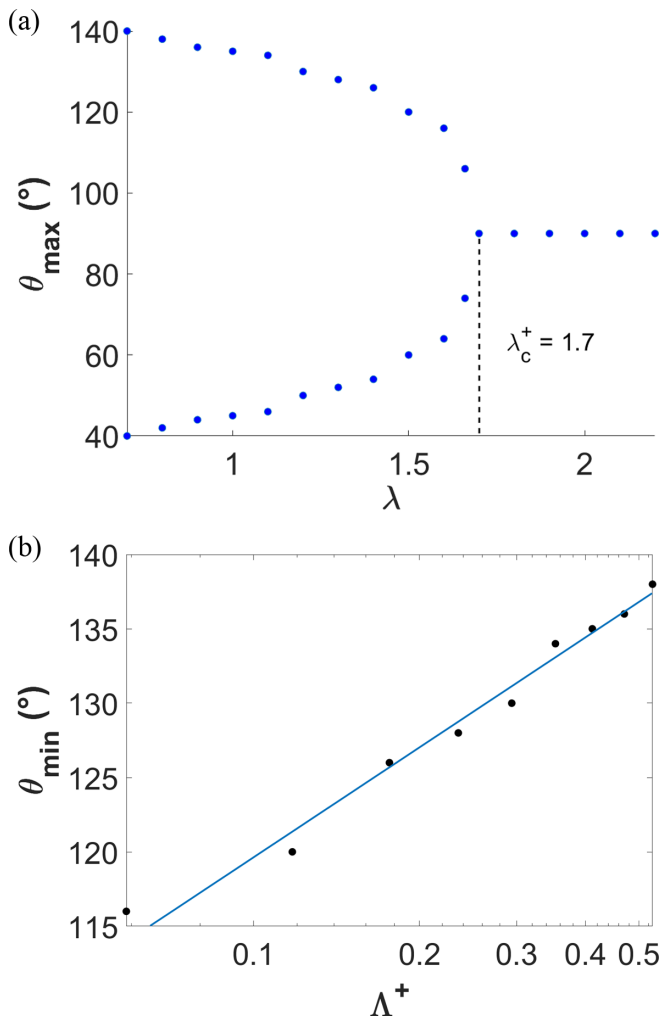


FIG. 26. Evolution of  $\theta_{\max}$  (degrees) for the case of cubic lattice ( $32 \times 32 \times 32$ ). (a)  $\theta_{\max}$  (degrees) relative to  $\lambda$ . (b)  $\theta_{\max}$  (degrees), in semi-log  $x$  scale, relative to  $\Lambda^+$ :  $\theta_{\max}$  fits with the linear regression (blue curve) here with a slope  $\beta^+ = 0.082 \pm 0.018$ , suggesting the power law  $\theta_{\max} \sim (\Lambda^+)^{\beta^+}$ .

power law almost parabolic relative to  $\lambda$  (with a positive slope). The system size-dependence of this energy barrier has also been found to follow a power law with an exponent,  $\kappa = 0.25 \pm 0.14$ , for large sizes. As for the second-order phase transition, of  $\theta_{\min}$  vs  $\lambda$ , various critical exponents have been determined: (i)  $\beta = 0.0844 \pm 0.0030$  exponent characterising the behavior of  $\theta_{\min} \sim \Lambda^\beta$  and (ii)  $\nu = 0.63 \pm 0.25$  characterising the behavior of the correlation length  $\xi \sim \Lambda^{-\nu}$ , where  $\Lambda = (\lambda - \lambda_c)/\lambda_c$  is the reduced anisotropic ratio and  $\lambda_c$  is the critical point. These values of the critical exponents have been corroborated by a finite size scaling analysis, and overall these critical exponents seem to fall in the universality class of the four-state bidimensional Potts model. It seems that there

is a close relation between the stable interface orientations  $\theta_{\min}$ ,  $\pi + \theta_{\min}$ ,  $-\theta_{\min}$  and  $-\pi - \theta_{\min}$ , and the value of the critical exponent which suggests the four states Potts model. However, for a complete study, one needs to evaluate the other critical exponents to confirm this assumption.

Finally, we evidenced an unusual behavior for the preferential orientation  $\theta_{\min}$  of the HS-LS interface for stripe bidimensional-like system size ( $192 \times 48 \times 16$ ). The stable interface is tilted ( $\theta_{\min} \neq 90^\circ$ ) with two symmetric stable orientations for  $\lambda < \lambda_c^- < 0$ , then changes to a straight one ( $\theta_{\min} = 90^\circ$ ) for  $\lambda_c^- < \lambda < \lambda_c^+$ , where  $\lambda_c^+ > 0$  and finally becomes again tilted for  $\lambda > \lambda_c^+$ . In this behavior of re-entrant phase transition with two successive “classical” second-order-like phase transitions, where in the 2nd one the order parameter experiences a bifurcation point and behaving as  $\theta_{\min} \sim (\Lambda^+)^{\beta^+}$  where  $\Lambda^+ = (\lambda - \lambda_c^+)/\lambda_c^+$  with  $\beta^+ = 0.14 \pm 0.02$ , which could naively be compared to the value of the critical exponent of the 2D Ising model ( $\beta = 1/8$ ). This result might be attributed to the stripe bidimensional-like shape of the studied system, leading to a lattice size along the  $z$  direction which is probably smaller than the correlation length. However, additional extensive investigations should be carried out to confirm this conjecture.

Overall, the present results highlight the role of the unit cell deformation (isotropic/anisotropic) along the spin transition in the emergence of the macroscopic interface as well as in the release of the elastic strain at the interface. When the unit cell expands or contracts isotropically in the three directions, the elastic energy depicts a single minimum with the interface orientation where strong elastic strain subsists in the vicinity of the HS-LS interface where the large part of the elastic energy due to volume misfit is stored, explaining the deterioration of the SCO crystals in most of the experiments. In contrast, when the unit cell stretches in the anisotropic way, there exists a preferential orientation of the interface that almost cancels the elastic strain due to the lattice parameter misfit, thus explaining the robust character of the crystals showing tilted HS-LS interfaces. Thus understanding the fundamental mechanism leading to minimize the stress along the spin transition is of high importance for their potential applications as re-usable reversible memories and sensors. These concepts are very general and can be applied to other families of switchable materials such as Prussian blue analogs and thermosolient materials etc.

## ACKNOWLEDGMENTS

We gratefully acknowledge Universities of Versailles and Paris-Saclay, CNRS (“Centre National de la Recherche Scientifique”), LIA France-Japan and ANR (Agence Nationale de la Recherche Scientifique) Grant No. Mol-CoSM ANR-20-CE07-0028-02, for their financial support. The authors declare neither conflict of interest nor competing financial interest.

[1] P. Gütllich and H. Goodwin, Spin crossover—An overall perspective, in *Spin Crossover in Transition Metal Compounds I*, edited by P. Gütllich and H. Goodwin, Topics in Current Chemistry Vol. 233 (Springer, Berlin, Heidelberg, 2004), pp. 1–47.

[2] P. Gütllich, A. Hauser, and H. Spiering, Thermal and optical switching of iron(II) complexes, *Angew. Chem. Int. Ed. Engl.* **33**, 2024 (1994).

[3] O. Kahn and J.-P. Launay, Molecular bistability: An overview, *J. P. Chemtronics* **3**, 140 (1988).

- [4] Y. Garcia and P. Gütllich, Thermal spin crossover in Mn(II), Mn(III), Cr(II) and Co(III) coordination compounds, in *Spin Crossover in Transition Metal Compounds II*, edited by P. Gütllich and H. Goodwin, Topics in Current Chemistry Vol. 49 (Springer, Berlin, Heidelberg, 2004).
- [5] A. Slimani, F. Varret, K. Boukheddaden, C. Chong, H. Mishra, J. Haasnoot, and S. Pillet, Visualization and quantitative analysis of spatiotemporal behavior in a first-order thermal spin transition: A stress-driven multiscale process, *Phys. Rev. B* **84**, 094442 (2011).
- [6] P. Gütllich, A. B. Gaspar, V. Ksenofontov, and Y. Garcia, Pressure effect studies in molecular magnetism, *J. Phys.: Condens. Matter* **16**, S1087 (2004).
- [7] K. Boukheddaden, M. H. Ritti, G. Bouchez, M. Sy, M. M. Dîrtu, M. Parlier, J. Linares, and Y. Garcia, Quantitative contact pressure sensor based on spin crossover mechanism for civil security applications, *J. Phys. Chem. C* **122**, 7597 (2018).
- [8] J. Linares, E. Codjovi, and Y. Garcia, Pressure and temperature spin crossover sensors with optical detection, *Sensors* **12**, 4479 (2012).
- [9] A. Bousseksou, N. Negre, M. Goiran, L. Salmon, J. P. Tuchagues, M. L. Boillot, K. Boukheddaden, and F. Varret, Dynamic triggering of a spin-transition by a pulsed magnetic field, *Eur. Phys. J. B* **13**, 451 (2000).
- [10] Y. Ogawa, T. Ishikawa, S. Koshihara, K. Boukheddaden, and F. Varret, Effect of the magnetic field on the dynamics of the cooperative photoinduced spin-state transition and relaxation, *Phys. Rev. B* **66**, 073104 (2002).
- [11] A. Desaix, O. Roubeau, J. Jeftic, J. Haasnoot, K. Boukheddaden, E. Codjovi, J. Linares, M. Nogues, and F. Varret, Light-induced bistability in spin transition solids leading to thermal and optical hysteresis, *Eur. Phys. J. B* **6**, 183 (1998).
- [12] A. Hauser, J. Jeftic, H. Romstedt, R. Hinek, and H. Spiering, Cooperative phenomena and light-induced bistability in iron(ii) spin-crossover compounds, *Coord. Chem. Rev.* **190-192**, 471 (1999).
- [13] F. Varret, C. Chong, A. Goujon, and K. Boukheddaden, Light-induced phase separation (LIPS) in  $[\text{Fe}(\text{ptz})_6](\text{BF}_4)_2$  spin-crossover single crystals: Experimental data revisited through optical microscope investigation, *J. Phys.: Conf. Ser.* **148**, 012036 (2009).
- [14] M. Sy, R. Traiche, H. Fourati, Y. Singh, F. Varret, and K. Boukheddaden, Spatiotemporal investigations on light-driven high-spin–low-spin interface dynamics in the thermal hysteresis region of a spin-crossover single crystal, *J. Phys. Chem. C* **122**, 20952 (2018).
- [15] O. Fouche, J. Degert, G. Jonusauskas, N. Daro, J.-F. Létard, and E. Freysz, Mechanism for optical switching of the spin crossover  $[\text{Fe}(\text{NH}_2\text{-trz})_3](\text{Br})_2 \cdot 3\text{H}_2\text{O}$  compound at room temperature, *Phys. Chem. Chem. Phys.* **12**, 3044 (2010).
- [16] A. Hauser, Spin-crossover materials. Properties and applications, *Angew. Chem. Int. Ed.* **52**, 10419 (2013).
- [17] C. Jureschi, J. Linares, A. Rotaru, M.-H. Ritti, M. Parlier, M. Dîrtu, M. Wolff and Y. Garcia, Pressure sensor via optical detection based on a 1D spin transition coordination polymer, *Sensors* **15**, 2388 (2015).
- [18] H. Shepherd, P. Rosa, I. Fallis, P. Guionneau, J. Howard, and A. Goeta, Structural origin of the gradual spin transition in a mononuclear iron(II) complex, *J. Phys. Chem. Solids* **73**, 193 (2012).
- [19] K. Takahashi, H. Mori, H. Kobayashi, and O. Sato, Mechanism of reversible spin transition with a thermal hysteresis loop in  $[\text{Fe}^{\text{III}}(\text{qsal})_2][\text{Ni}(\text{dmise})_2] \cdot 2\text{CH}_3\text{CN}$ : Selenium analogue of the precursor of an Fe(III) spin-crossover molecular conducting system, *Polyhedron* **28**, 1776 (2009).
- [20] C. Enachescu, J. Linares, and F. Varret, Comparison of static and light-induced thermal hystereses of a spin-crossover solid, in a mean-field approach, *J. Phys.: Condens. Matter* **13**, 2481 (2001).
- [21] K. Boukheddaden, I. Shteto, B. Hôo, and F. Varret, Dynamical model for spin-crossover solids. I. Relaxation effects in the mean-field approach, *Phys. Rev. B* **62**, 14796 (2000).
- [22] W. Nicolazzi, and S. Pillet, Structural aspects of the relaxation process in spin crossover solids: Phase separation, mapping of lattice strain, and domain wall structure, *Phys. Rev. B* **85**, 094101 (2012).
- [23] M. Nishino, T. Nakada, C. Enachescu, K. Boukheddaden, and S. Miyashita, Crossover of the roughness exponent for interface growth in systems with long-range interactions due to lattice distortion, *Phys. Rev. B* **88**, 094303 (2013).
- [24] A. Slimani, K. Boukheddaden, F. Varret, H. Oubouchou, M. Nishino, and S. Miyashita, Microscopic spin-distortion model for switchable molecular solids: Spatiotemporal study of the deformation field and local stress at the thermal spin transition, *Phys. Rev. B* **87**, 014111 (2013).
- [25] M. Ndiaye and K. Boukheddaden, Electro-elastic modelling of the two-step high-spin to low-spin relaxation with transient self-organized spin states in 2D spin crossover solids, *J. Phys. Soc. Jpn.* **89**, 014004 (2020).
- [26] C. Chong, H. Mishra, K. Boukheddaden, S. Denise, G. Bouchez, E. Collet, J.-C. Ameline, A. D. Naik, Y. Garcia, and F. Varret, Electronic and structural aspects of spin transitions observed by optical microscopy. The case of  $[\text{Fe}(\text{ptz})_6](\text{BF}_4)_2$ , *J. Phys. Chem. B* **114**, 1975 (2010).
- [27] A. Slimani, F. Varret, K. Boukheddaden, D. Garrot, H. Oubouchou, and S. Kaizaki, Velocity of the High-Spin Low-Spin Interface Inside the Thermal Hysteresis Loop of a Spin-Crossover Crystal, via Photothermal Control of the Interface Motion, *Phys. Rev. Lett.* **110**, 087208 (2013).
- [28] K. Ridier, G. Molnar, L. Salmon, W. Nicolazzi, and A. Bousseksou, Hysteresis, nucleation and growth phenomena in spin-crossover solids, *Solid State Sci.* **74**, A1 (2017).
- [29] M. Nishino, K. Boukheddaden, Y. Konishi, and S. Miyashita, Simple Two-Dimensional Model for the Elastic Origin of Cooperativity among Spin States of Spin-Crossover Complexes, *Phys. Rev. Lett.* **98**, 247203 (2007).
- [30] C. Enachescu, L. Stoleriu, A. Stancu, and A. Hauser, Model for Elastic Relaxation Phenomena in Finite 2D Hexagonal Molecular Lattices, *Phys. Rev. Lett.* **102**, 257204 (2009).
- [31] M. Nishino, C. Enachescu, S. Miyashita, P. A. Rikvold, K. Boukheddaden, and F. Varret, Macroscopic nucleation phenomena in continuum media with long-range interactions, *Sci. Rep.* **1**, 162 (2011).
- [32] C. Enachescu and W. Nicolazzi, Elastic models, lattice dynamics and finite size effects in molecular spin crossover systems, *C. R. Chim.* **21**, 1179 (2018).

- [33] M. Nishino, Y. Singh, K. Boukheddaden, and S. Miyashita, Tutorial on elastic interaction models for multistep spin-crossover transitions, *J. Appl. Phys.* **130**, 141102 (2021).
- [34] K. Boukheddaden and A. Bailly Reyre, Towards the elastic properties of 3D spin-crossover thin films: evidence of buckling effects, *Europhys. Lett.* **103**, 26005 (2013).
- [35] L. Stoleriu, M. Nishino, S. Miyashita, A. Stancu, A. Hauser, and C. Enachescu, Cluster evolution in molecular three-dimensional spin-crossover systems, *Phys. Rev. B* **96**, 064115 (2017).
- [36] A.-I. Popa, L. Stoleriu, and C. Enachescu, Tutorial on the elastic theory of spin crossover materials, *J. Appl. Phys.* **129**, 131101 (2021).
- [37] N. di Scala, N. E. I. Belmouri, M. Paez Espejo and K. Boukheddaden, Three-dimensional electroelastic modeling of the nucleation and propagation of the spin domains in spin-crossover materials, *Phys. Rev. B* **106**, 014422 (2022).
- [38] M. Paez-Espejo, M. Sy, and K. Boukheddaden, Unprecedented bistability in spin-crossover solids based on the retroaction of the high spin low-spin interface with the crystal bending, *J. Am. Chem. Soc.* **140**, 11954 (2018).
- [39] M. Sy, F. Varret, K. Boukheddaden, G. Bouchez, J. Marrot, S. Kawata, and S. Kaizaki, Structure-driven orientation of the high-spin–low-spin interface in a spin-crossover single crystal, *Angew. Chem. Int. Ed.* **53**, 7539 (2014).
- [40] M. Sy, D. Garrot, A. Slimani, M. Paez-Espejo, F. Varret, and K. Boukheddaden, Reversible control by light of the high-spin low-spin elastic interface inside the bistable region of a robust spin-transition single crystal, *Angew. Chem.* **128**, 1787 (2016).
- [41] R. Traiche, M. Sy, H. Oubouchou, G. Bouchez, F. Varret, and K. Boukheddaden, Spatiotemporal observation and modeling of remarkable temperature scan rate effects on the thermal hysteresis in a spin-crossover single crystal, *J. Phys. Chem. C* **121**, 11700 (2017).
- [42] K. Boukheddaden, H. Fourati, Y. Singh, and G. Chastanet, Evidence of photo-thermal effects on the first-order thermo-induced spin transition of  $[\text{Fe}(\text{NCSe})(\text{py})_2(\text{m-bpypz})]$  spin-crossover material, *Magnetochemistry* **5**, 21 (2019).
- [43] K. Boukheddaden, M. Sy, M. Paez-Espejo, A. Slimani, and F. Varret, Dynamical control of the spin transition inside the thermal hysteresis loop of a spin-crossover single crystal, *Phys. B: Condens. Matter* **486**, 187 (2016).
- [44] M. Nadeem, J. Cruddas, G. Ruzzi, and B. J. Powell, Toward high-temperature light-induced spin-state trapping in spin-crossover materials: The interplay of collective and molecular effects, *J. Am. Chem. Soc.* **144**, 9138 (2022).
- [45] NVIDIA, CUDA, Retrieved from <https://developer.nvidia.com/cuda-toolkit>
- [46] J. Jung, F. Bruchhäuser, R. Feile, H. Spiering, and P. Gütllich, The cooperative spin transition in  $[\text{F}_x\text{Zn}_{1-x}(\text{ptz})_6](\text{BF}_4)_2$ : I. Elastic properties—an oriented sample rotation study by Brillouin spectroscopy, *Z. Phys. B* **100**, 517 (1996).
- [47] I. G. Enting, Critical exponents for the four-state Potts model, *J. Phys. A: Math. Gen.* **8**, L35 (1975).
- [48] R. H. Swendsen, D. Andelman, and A. N. Berker, Critical exponents and marginality of the four-state Potts model: Monte Carlo renormalization group, *Phys. Rev. B* **24**, 6732 (1981).
- [49] S. Miyashita, Y. Konishi, M. Nishino, H. Tokoro, and P. A. Rikvold, Realization of the mean-field universality class in spin-crossover materials, *Phys. Rev. B* **77**, 014105 (2008).
- [50] M. Nishino, K. Boukheddaden, and S. Miyashita, Molecular dynamics study of thermal expansion and compression in spin-crossover solids using a microscopic model of elastic interactions, *Phys. Rev. B* **79**, 012409 (2009).
- [51] See Supplemental Material at <http://link.aps.org/supplemental/10.1103/PhysRevB.106.144107> for (i) two movies showing the spatial distribution of the local pressure field through the lattice during the relaxation process at different orientation angles and (ii) two figures, the first one showing the time-dependence of the average local pressure calculated through the whole lattice for  $\lambda = -0.6$  and  $\theta_{\text{max}} = 90^\circ$ , and the second one showing  $\Delta E$  fits with the linear regression (blue curve) here with a slope  $\kappa \approx 0.5035$ , suggesting the power law  $\Delta E \sim (N_x)^\kappa$  for  $\lambda = -0.6$ .